Expanded FLP toolbox for spatiotemporal protein degradation and transcriptomic profiling in *C. elegans*

Adrián Fragoso-Luna[1,4], Cristina Ayuso[1,4], Michael Eibl[1,4], Celia Muñoz-Jiménez[1], Vladimir Benes[2], Ildefonso Cases[1], Peter Askjaer[3]

[1] Andalusian Centre for Developmental Biology, Consejo Superior de Investigaciones Científicas (CSIC), Universidad Pablo de Olavide, Junta de Andalucía, Carretera de Utrera, km 1, 41013 Sevilla, Spain

[2] EMBL GeneCore, Meyerhofstrasse 1, 69117 Heidelberg, Germany

[3] Corresponding author (pask@upo.es)

[4] These authors contributed equally

Keywords: FLP/FRT recombination; GFPdeg; SLAM-ITseq; spatiotemporal gene expression control; targeted protein degradation

Abstract

Control of gene expression in specific tissues and/or at certain stages of development allows the study and manipulation of gene function with high precision. Site-specific genome recombination by the Flippase (FLP) and Cre enzymes has proven particularly relevant. Joint efforts of many research groups have led to the creation of efficient FLP and Cre drivers to regulate gene expression in a variety of tissues in *Caenorhabditis elegans*. Here, we extend this toolkit by the addition of FLP lines that drive recombination specifically in distal tip cells, the somatic gonad, coelomocytes and the epithelial P lineage. In some cases, recombination-mediated gene knockouts do not completely deplete protein levels due to persistence of long-lived proteins. To overcome this, we developed a spatiotemporally regulated degradation system for GFP fusion proteins (GFPdeg) based on FLP-mediated recombination. Using two stable nuclear pore proteins, MEL-28/ELYS and NPP-2/NUP85 as examples, we report the benefit of combining tissue-specific gene knockout and protein degradation to achieve complete protein depletion. We also demonstrate that FLP-mediated recombination can be utilized to identify nascent transcripts in a tissue of interest. We have adapted thiol(SH)-linked alkylation for the metabolic sequencing of RNA in tissue (SLAM-ITseq) for *C. elegans*. By focusing on a well-characterized tissue, the hypodermis, we show that the vast majority of genes identified by SLAM-ITseq are known to be expressed in this tissue, but with the added value of temporal resolution. These tools allow combining FLP activity for simultaneous gene inactivation and transcriptomic profiling, thus enabling the inquiry of gene function in various complex biological processes.

Introduction

The nematode *C. elegans* is a popular model organism for genetic and biomedical research. A variety of methods have been developed to perturb gene expression and protein abundance in specific tissues and/or at particular developmental stages of *C. elegans*. These include tissue-specific RNA interference (RNAi) [1], conditional protein degradation [2-4] and site-specific recombinases [5,6]. Especially Cyclization recombination (Cre) and Flippase (FLP) enzymes are popular tools for the control of gene expression in a spatiotemporal manner [7,5]. While Cre was derived from the P1 bacteriophage [8], FLP originates from *Saccharomyces cerevisiae* [9]. The Cre and FLP recombinases recognize 34 bp sequences, that are called loxP (locus of crossing-over in P1) and FRT (FLP recognition target), respectively. DNA located between two target sequences is either excised or inverted depending on their orientation. Both systems have been used efficiently in *C. elegans*, for example to induce gene knockout (KO) [10,11], control ectopic expression [12], ablation of neurotransmission [13], determination of gene expression [14], mapping of chromatin organization [15,16] and transgenesis [17]. Moreover, by utilizing both Cre and FLP, further versatility and cell specificity can be achieved [18,17]. Thanks to community efforts, a growing number of characterized and stable Cre and FLP drivers are available, which facilitates the development and implementation of recombination-based tools [19,11,20-23]. Most recently, a light-inducible Cre recombinase has been added to the toolbox [24].

In some cases, the study of gene function at specific developmental time points can be compromised by remaining protein levels after gene perturbation. At a time point of interest, remaining protein might occlude the true phenotype associated with the gene's loss of function by RNAi or conditional KO. This may be particularly relevant for long-lived proteins, such as histones and nuclear pore complex (NPC) proteins, that sometimes show lifelong persistence [25,26]. Besides, re-initiation of translation in the case of frameshift-mediated KO appears to be more prevalent than previously anticipated [27]. The combination of gene KO methods with conditional protein degradation may help to overcome this hurdle and completely deplete protein levels.

Tools for targeted protein degradation are constantly being developed and adapted for *C. elegans* and other model organisms [6]. Auxin-inducible degradation (AID) of proteins tagged with a 44 amino acid AID degron offers both temporal and spatial control through exposure to auxin and expression of *Arabidobsis thaliana* TIR1 protein, respectively [2]. Wang et al. [3] developed a system for the degradation of green fluorescent protein (GFP)-tagged proteins in *C. elegans* building on previous protein depletion systems [28,29]. In this GFP degradation (GFPdeg) system, a camelid single-domain antibody fragment that specifically binds GFP ("GFP nanobody") is fused to the SOCS-box adaptor protein ZIF-1, that recruits CUL-2/Cullin-2, an E3 ligase. This leads to ubiquitination and proteasomal degradation of the GFP-tagged protein. An advantage of GFPdeg is that it is immediately applicable to any existing line expressing a GFP-tagged protein, but it offers only spatial control in its current version. Degradation kinetics in the AID or GFPdeg systems depend on the synthesis and turnover rates of the target protein, which sometimes renders protein depletion incomplete. Therefore, using AID or GFPdeg on its own may also not be sufficient for the inquiry of some biological processes and could benefit from the combination with genetic tools, such as site-specific recombination.

Here, we report an extension of the FLP-based toolbox for *C. elegans* by four means. Firstly, we describe novel integrated single-copy FLP drivers that efficiently induce recombination in the somatic gonad, distal tip cells, the P lineage or coelomocytes. We also report an improved FLP driver for intestinal cells. These drivers increase the number of cell types amenable for easy FLP-mediated spatiotemporal control of gene expression. Secondly, we adapt the GFPdeg system for FLP-based regulation, thereby enabling spatiotemporal control of GFP fusion protein degradation. We show that inducible GFPdeg is equally efficient as the original constitutive version. Thirdly, using two endogenously GFP-tagged nuclear pore proteins, MEL-28/ELYS and NPP-2/NUP85, as test cases, we provide evidence that combined FLP-mediated gene KO and protein degradation is rapid and highly efficient to deplete stable proteins from a specific tissue of interest. The possibility of using a single FLP driver to control both conditional gene KO and protein degradation will facilitate the inquiry of tissue-specific gene function in complex biological processes. Lastly, we present the application of thiol(SH)-linked alkylation for the metabolic sequencing of RNA in tissue (SLAM-ITseq) in *C. elegans*. This powerful method for identification of nascent transcripts in a spatiotemporal specific manner was recently developed for gene expression analysis in mice [30]. We show here that SLAM-ITseq can identify nascent transcripts in the hypodermis of L4 larvae without the need of physical isolation of cells. We propose that combined with the growing list of tissue-specific FLP drivers, SLAM-ITseq can be used to explore transcription profiles across tissues and developmental progression.

Material and Methods

Plasmids

Promoter fragments for FLP expression constructs were PCR-amplified with *Pfu* polymerase using wild type *C. elegans* genomic DNA as template and inserted as *Not*I/*Kpn*I fragments into *Not*I/*Kpn*I of plasmid pBN338 [20]. Details are in Supplementary Tables S2 and S3. Exceptions were (1) pBN527 *gpa-14p::FLP::SL2::mNG* that was generated by first combining a 2.4 kb *Not*I/*Cla*I restriction fragment from pNP259 [12] with a 0.6 kb *Cla*I/*Kpn*I PCR fragment followed by insertion into *Not*I/*Kpn*I of pBN338 and (2) pBN487 *unc-122p::FLP::SL2::mNG* that was generated by inserting a *Not*I/*BsrG*I PCR fragment into *Not*I/*Acc65*I of pBN338. For generation of pBN532 *hlh-12p::FLP::SL2::mTagBFP2*, an intergenic *gpd-2/-3* sequence was amplified with primers B1012 and B1364 (see Supplementary Table S1) using pBN338 as template. A sequence encoding mTag2BFP2 was amplified with B1365 and B1366 using pMINIT mTagBFP2 [31] as template. The two PCR fragments were PCR-stitched with primers B1012 and B1366 and inserted by NEBuilder HiFi DNA Assembly (New England Biolabs) into *Mlu*I of pBN523.

Targeting plasmids for SapTrap CRISPR/Cas9 gene modification were obtained as described [32]. Details for construction of plasmids pBN309 *mCh::baf-1*, pBN433 *g>f>p::npp-2* (">" denotes an FRT site) and pBN493 *gf>p::baf-1* are provided in Supplementary Tables S1 and S3. Plasmid pBN351 for insertion of *g>f>p* in the 5'-end of the endogenous *mel-28* open reading frame was generated from plasmids pMLS256, pMLS288 and pBN312 [32,20], sgRNA oligonucleotides B1050 and B1051, 5' homology arm (499 bp; amplified with B1042 and B1043 using plasmid #1397 [33] as template) and 3' homology arm (258 bp; amplified with B1044 and

139 B1045 using plasmid #1397 as template) (see Supplementary Tables S1 and S3).
140 Donor plasmid pBN477 containing FRT in the second *gfp* intron was constructed by
141 inserting a 574 bp *Xho*I/*Hin*dIII fragment from pBN312 into *Xho*I/*Hin*dIII of pMLS252
142 [32].

143 Plasmid pBN452 *hsp16.41p>mCh::his-58>HA::UPRT* for SLAM-ITseq was
144 generated by Gibson assembly (New England Biolabs) using gBlocks B1275 and
145 B1276 (Supplementary Table S1) and plasmid pBN209 *hsp16.41p>mCh::his-*
146 *58>dam::emr-1* [15] digested with *Xho*I and *Nhe*I to replace *dam::emr-1*. The
147 sequence of HA::UPRT was codon optimized for *C. elegans* [34] and gBlocks were
148 purchased from IDT.

149 Plasmid pBN488 *hsp16.41p>mCh::his-58>vhhGFP4::zif-1* for targeted degradation
150 of GFP fusion proteins was constructed by amplifying *vhhGFP4::zif-1* with primers
151 B1333 and B1334 using plasmid pNH102 (a kind gift from Ngang Heok Tang and
152 Andrew Chisholm) as template. The PCR product was digested with *Xho*I and *Nhe*I
153 and inserted into pBN452 digested with the same enzymes to replace *HA::UPRT*.

154 *Nematode culture, strains and genome engineering*

155 Worm strains were maintained on Nematode Growth Medium (NGM) petri dishes
156 seeded with *Escherichia coli* OP50 [35]. Unless otherwise noted, strains were
157 maintained at 16°C. The N2 strain was used as wild type reference. Other strains
158 are listed in Supplementary Table S4.

159 Single-copy insertion of FLP expression constructs into the *cxTi10882* locus on chrIV
160 was done by microinjection into the gonads of EG6700 young adult hermaphrodites
161 [36,37]. Plasmids carrying FLP and *unc-119(+)* as selection marker were injected at
162 50 ng/µl together with pCFJ601 *eft-3p::Mos1* ([38], 50 ng/µl), pBN1 *lmn-*
163 *1p::mCh::his-58* ([39], 10 ng/µl), pCFJ90 *myo-2p::mCh* ([36], 2.5 ng/µl) and pCFJ104
164 *myo-3p::mCh* ([36], 5 ng/µl). Integration of the FLP expression constructs was
165 confirmed by detection of fluorescent mNeonGreen (mNG) or mTagBFP2 in the
166 target tissue of wild-type moving animals without ectopic mCherry expression from
167 the co-injection markers.

168 Similarly, single-copy insertion of HA::UPRT and vhhGFP4::ZIF-1 expression
169 constructs into the *ttTi5605* locus on chrII was done by microinjection into the
170 gonads of EG4322 young adult hermaphrodites. Injection markers and transposase
171 plasmid were injected at same concentrations as above. Integrity of the integrated
172 transgenes was confirmed by PCR, and, after crossing to FLP drivers, functional
173 assays (degradation of GFP fusion proteins for the GFPdeg system; see Confocal
174 Microscopy below) and western blotting (for HA::UPRT). For Western blotting,
175 nematodes were lysed in SDS sample buffer and extracts were loaded on BioRad
176 TGX Stain-Free 12% polyacrylamide gels followed by visualization on a
177 ChemiDocTM MP Imaging System. Proteins were then transferred to membranes
178 and probed with Covance #MMS-101R Anti-HA.11 Epitope Tag Antibody.

179 CRISPR/Cas9-mediated genome modification to generate strains BN581 *baf-*
180 *1(bq13[mCh::baf-1])* III, BN1164 *baf-1(bq47[gf>p::baf-1])* III, BN902 *mel-*
181 *28(bq17[g>f>p::mel-28])* III and BN1044 *npp-2(bq38[g>f>p::npp-2])* I was performed
182 by microinjection of targeting plasmids pBN309, pBN493, pBN351 and pBN433,
183 respectively, into the gonads of HT1593 *unc-119(ed3)* III young adult
184 hermaphrodites [32]. Targeting plasmids were injected at 65 ng/µl together with
185 plasmids #1286 *eft-3p::Cas9* ([40], 25 ng/µl), pBN1 (10 ng/µl), pCFJ90 (2.5 ng/µl)

186 and pCFJ104 (5 ng/µl). Successful modification of the target loci was confirmed by
187 detection of fluorescent fusion proteins in the nuclear envelope throughout the body
188 of wild-type moving animals without ectopic mCherry expression from the co-
189 injection markers. The *unc-119(+)* selection marker was next excised by
190 microinjection with Cre expression plasmid pMLS328 [32]. Finally, uncoordinated
191 hermaphrodites were outcrossed to N2 males to remove the *unc-119(ed3)* allele.

192 Insertion of an FRT in the *baf-1* 3'-UTR was performed by microinjection of BN1164
193 *baf-1(bq47[gf>p::baf-1])* young adult hermaphrodites with a mixture containing 10 µM
194 *baf-1* crRNA:trRNA duplex (B1312+B1067), 2.5 µM *dpy-10* crRNA:trRNA duplex
195 (B1068+B1067), 3 µM recombinant Cas9, 4 µM *baf-1* ssDNA repair template
196 (B1313) and 1 µM *dpy-10* ssDNA repair template (B725). Recombinant Cas9 was
197 produced by the CABD Proteomics and Biochemistry Facility. All DNA and RNA
198 oligonucleotides were purchased from IDT.

199 *Confocal microscopy*

200 To induce expression of either the dual-color FRT reporter or the GFPdeg system,
201 NGM plates with nematodes were incubated for 15 min floating in a 34°C water bath.
202 For evaluation of recombination efficiency and specificity, nematodes were left to
203 recover at 20°C for 2-3 hours prior to imaging. For GFP degradation experiments,
204 recovery was at 25°C for 1-24 hours as indicated for each experiment. For imaging,
205 nematodes were anesthetized in 5 µl 10 mM levamisole HCl on 2% agarose pads
206 and covered by a cover slip. Images were acquired with a Nikon Eclipse Ti
207 microscope equipped with Plan Fluor 40×/1.3 and Plan Apo VC 60×/1.4 objectives
208 and an A1R scanner using a pinhole of 1.2 airy units [20]. Cells with GFP signal as
209 an indication of a recombination event in the dual-color reporter as well as mNG co-
210 expression with FLP were evaluated from z-stacks acquired with the Nikon NIS
211 software. To analyze the reduction of protein levels of GFP fusion proteins after FLP
212 recombination and/or the induction of the GFP degradation system, specific regions
213 and focal planes were localized to acquire reproducible sets of images. These are
214 indicated in the text.

215 Fluorescence intensity was quantified in Fiji/ImageJ 2.1.0/1.53c [41] by tracing and
216 measuring the signal at the nuclear envelope with a freehand line of width 3. After
217 subtracting the background measured in animals without expression of GFP, the
218 data were analyzed in R Studio (1.3.1093 [42]; running R 4.0.2 [43]). Data were
219 visualized either with base plotting or using ggplot2 [44], mainly within the ggpubr
220 framework (version 0.4.0 [45]). For statistical analysis, Wilcoxon rank sum tests were
221 performed within the ggpubr framework and adjusted for multiple comparison
222 (Benjamini & Hochberg method).

223 *Brood size experiments*

224 BN580 *g>f>p::baf-1*, BN1182 *mCh::baf-1/g>f>p::baf-1; nhx-2p::FLP* and BN1223
225 *mCh::baf-1/gf>p::baf-1>; nhx-2p::FLP* worms were cultured at 16°C until L4 larval
226 stage. For BN1182 and BN1223, homozygous *mCh::baf-1*, *g>f>p::baf-1* and
227 *gf>p::baf-1>* animals were selected under a fluorescence stereoscope. In each
228 replica, 8-10 L4 larvae per strain were transferred to individual NGM plates and
229 incubated at 20°C. During the reproductive period, adults were transferred to new
230 plates each day and the number of progenies were recorded. Adults were censored
231 if they desiccated on the walls of the plates or were damaged during transfer.

232 Statistical analysis was done in R using Wilcoxon rank sum tests and adjusted for
233 multiple comparison (Benjamini & Hochberg method).

234 *Lifespan experiments*

235 Worms were cultured at 16°C until L4 larval stage. In each replica, 20 L4 larvae per
236 strain were transferred to newly seeded NGM plates and incubated for 15 min
237 floating in a 34°C water bath to induce the GFPdeg system. They were then
238 continuously incubated at 25°C. During the reproductive period, the live adults were
239 transferred to new plates each day to not confuse founders with their progeny.
240 Throughout the experiment, the number of live and dead animals were recorded.
241 Animals were censored if they disappeared, were damaged during transfer or died
242 due to internal hatching. Statistical analysis was done in R using the survival
243 package (version 3.2-7 [46]), which calculates Chi-square statistics based on a log-
244 rank test.

245 *SLAM-ITseq*

246 Eggs were obtained by sodium hypochlorite treatment [35] and incubated in M9
247 containing 0.01% Tween-20 (M9-T) overnight at 18°C without food. For each strain
248 and replica, three 60 mm NGM plates with a lawn of OP50 *E. coli* were seeded each
249 with approximately 350 synchronized L1 larvae and incubated at 20°C for 28 h until
250 reaching L3 stage. At this point, 4-thiouracil (Sigma-Aldrich) dissolved at 200 mg/ml
251 in DMSO was diluted 1:100 in H_2O and 1 ml was added on top of each NGM plate.
252 Plates were left to dry in a laminar flow hood (~1 h) and incubated at 20°C for a total
253 of 17 h. L4 larvae were washed off the plates with M9-T, collected in 15 ml tubes and
254 washed three times in M9-T. Finally, worms were pelleted in 1.5 ml tubes (~1000
255 L4s per tube). The supernatant was aspired to leave ~50 µl and 500 µl Trizol was
256 added. Tubes were snap frozen in liquid nitrogen and stored at -80°C until used.

257 Samples were lysed in 5 freeze/thaw cycles (1 min in liquid nitrogen; 3 min in 37°C
258 shaker) and left for 3 min at RT. Then, 100 µl chloroform was added, tubes were
259 shaken vigorously for 15 seconds and left for 3 min at RT. After centrifugation at
260 12000 g, 4ºC for 15 min, the aqueous phases (~300 µl) were transferred to new
261 tubes containing 0.5 µl 0.1 M DTT and 0.5 µl 20 mg/ml glycogen. RNA was
262 precipitated by adding 250 µl isopropanol and centrifugation at 12000 g, 4ºC for 10
263 min. Supernatants were removed and pellets were washed in 500 µl EtOH 75%.
264 After centrifugation and removal of the supernatants, the pellets were left to dry for 5
265 min and resuspended in 20 µl 1 mM DTT. After incubation at 55ºC for 10 min,
266 residual DNA was digested by treatment with DNase I (New England Biolabs) in a
267 total volume of 50 µl at 37ºC for 10 min. DNase I was inactivated by addition of 0.5 µl
268 0.5 M EDTA. RNA was purified with Monach spin columns (New England Biolabs),
269 eluted in 20 µl 1 mM DTT and evaluated on a Nanodrop.

270 Alkylation of RNA was performed by incubating 1.5 µg RNA with 25 µl DMSO, 5 µl
271 0.1 M iodoacetamide (Sigma-Aldrich) and 5 µl 0.5 M sodium phosphate (pH 8.0) in a
272 total volume of 50 µl at 50ºC for 15 min. The reaction was stopped by adding 1 µl 1M
273 DTT. RNA was precipitated by adding 0.5 µl 20 mg/ml glycogen, 5 µl 3 M sodium
274 acetate (pH 5.2) and 180 µl 96% ethanol followed by incubation at -20ºC for 20 min
275 and centrifugation at 15000 g, 4ºC for 20 min. The supernatants were removed and
276 the pellets were washed in 180 µl 75% ethanol followed by centrifugation at 15000 g,
277 4ºC for 5 min. Again, supernatants were removed and pellets were left to dry for 5
278 min. RNA was resuspended in 15 µl H_2O, incubated at 55ºC for 8 min and evaluated

on a Nanodrop. NGS libraries were prepared and sequenced at EMBL GeneCore using a QuantSeq 3′ mRNA-Seq Library Prep Kit for Illumina (Lexogen) and a NextSeq 500 (Illumina).

Bioinformatics analysis was performed as outlined in [47] using SLAM-DUNK [48] (http://t-neumann.github.io/slamdunk/) with default parameters. The *tcount* output file was then loaded into R and Spearman correlation coefficients between genotypes and replicas were calculated for the cumulative coverage on all Ts in the 3'-UTR (*coverageOnTs*; an indicator for transcript abundance in the sample). The DESeq2 package [49] was used to test if *coverageOnTs* were different between BN1158 (-FLP) and BN1190 (+ FLP) samples. Next, the countdata package [50] was used to perform a beta-binomial test on *conversionsOnTs* (number of T>C conversions) and *coverageOnTs* values to calculate p values for conversion rates (*conversionsOnTs*/*coverageOnTs*) of individual transcripts comparing BN1158 (-FLP) and BN1190 (+ FLP) samples. To increase stringency, transcripts with <18 T>C reads (*conversionsOnTs*) were excluded and for genes represented by several transcripts, only the transcript with the lowest p value was retained. Finally, p values were adjusted for multiple comparison (Benjamini & Hochberg method).

Data availability

See Table S1, Table S2, Table S3 and Table S4 for complete lists of primers, promoters, plasmids and strains, respectively. Representative strains will be made immediately available through the *Caenorhabditis* Genetics Center; plasmids and other strains can be requested from the authors. Table S5 contains list of hypodermal genes identified by SLAM-ITseq. Raw and processed SLAM-ITseq files are deposited at Gene Expression Omnibus (https://www.ncbi.nlm.nih.gov/geo/).

Results

Characterization of new FLP lines

Previously, a series of efficient tissue-specific FLP-lines were generated by Mos1-mediated Single Copy Insertion (MosSCI) [20,22,23,51]. To expand the existing toolkit, we created additional MosSCI lines that express FLP in specific cell types and evaluated recombination efficiency with the heat-inducible dual color reporter *bqSi294* that produces green nuclei (GFP::HIS-58) upon successful recombination and red nuclei (mCherry::HIS-58) elsewhere (Figure 1A) [20]. In most constructs (see below), an SL2 trans-splicing sequence followed by the gene encoding the fluorescent protein mNeonGreen (mNG) was inserted downstream of FLP (FLP::SL2::mNG), enabling visualization of FLP expression by co-expression of mNG [20].

We first generated a line that expresses FLP under control of the *ckb-3* promoter, which is active in the Z1 and Z4 cells that compose the somatic gonadal primordium of the hermaphrodite in early L1 larvae [52]. When crossed with the dual color reporter, we detected recombination in all 36 L1 larvae analyzed; in 35 larvae both Z1 and Z4 expressed GFP::HIS-58, and one larva expressed GFP::HIS-58 in a single cell (Figure 1B; Table 1). The majority of Z1/Z4 cells expressed GFP::HIS-58 only, indicating that recombination had taken place at both alleles (67/72 cells = 93%), whereas both green and red histones were observed in 4 cells. Of note, there were never more than the expected two green nuclei at this developmental stage (early L1), which highlights the tissue specificity of the *ckb-3p::FLP* line. The high

326 efficiency of the line in the somatic gonadal primordium implies that it is very suitable
327 for manipulation of all five tissues of the reproductive system: distal tip cells, gonadal
328 sheath, spermatheca, spermatheca-uterine valve and the uterus (Figure 1B) [53].

329 The distal tip cells (DTCs) play important roles during development as the leading
330 cells that guide migration of the gonad arms in hermaphrodites and also in control of
331 germ cell proliferation [53]. To express FLP specifically in DTCs, we used the *hlh-12*
332 promoter which is expressed from L2 stage [54]. We observed recombination in both
333 DTCs in all hermaphrodites analyzed (*n*=24, L2-adult stage; Figure 1B; Table 1).
334 Except for one DTC in a young L2 larva, recombination had taken place at both
335 alleles (47/48 cells = 98%) and was not observed in other cell types, demonstrating
336 the high efficiency and specificity of the *hlh-12p::FLP* line.

337 We then generated a *lin-31p::FLP* line to enable recombination in the vulval
338 precursor cells (VPCs). LIN-31 is expressed in P1.p-P11.p cells from the middle of
339 L1 stage, when these cells are born [55]. We focused our attention on the central
340 VPCs in L2 larvae and on VPC descendants during vulval morphogenesis in L3 and
341 L4 larvae. Importantly, recombination of both alleles was observed in all VPCs and
342 VPC descendants in all animals (*n*=30, L2-adult stage; Figure 1B; Table 1). We also
343 observed GFP::HIS-58 expression in a few head neurons, which is in agreement
344 with a previous report on *lin-31* expression (Supplementary Figure S1A)[56]. Finally,
345 we noted weak GFP::HIS-58 signal in hyp7 nuclei in late L3-L4 larvae, which we
346 assume originates from fusion of descendants of P3.p, P4.p and P8.p with the hyp7
347 syncytium (Supplementary Figure S1A).

348 In the first version of our FLP toolkit, we used the *elt-2* promoter to drive
349 recombination in the intestine with ~100% efficiency [20]. However, because
350 recombination was also detected in the somatic gonad, we generated an alternative
351 line based on the *nhx-2* promoter [57]. In young L1 larvae, the number of intestinal
352 nuclei ranges from 19 to 22 and increases to 30-34 in L2 larvae [58]. Recombination
353 efficiency reached 98% based on green-only nuclei and 100% when also including
354 nuclei with expression of both green and red histones (*n*=27, Figure 1B; Table 1).
355 This demonstrates high recombination efficiency, comparable to the *elt-2p::FLP* line.
356 Importantly, we did not detect recombination outside the intestine with the *nhx-*
357 *2p::FLP* line, so we recommend to use this line.

358 We next generated an *unc-122p::FLP* line to enable recombination in coelomocytes
359 (CCs), which are specialized cells thought to be involved in the innate immune
360 response and scavenging [59,60]. Two anterior CC pairs are born during
361 embryogenesis whereas a posterior pair is born right before the L1/L2 molt.
362 Consistently, in 8 of 8 L1s we observed 4 GFP::HIS-58 expressing CCs, and in 23 of
363 23 L3-L4 larvae 6 GFP::HIS-58 expressing CCs (Figure 1B; Table 1). Expression of
364 mCh::HIS-58 was not detected in the CCs, indicating that both alleles had
365 recombined, whereas GFP::HIS-58 expression was restricted to the CCs.

366 We also attempted to generate additional lines to target specific neuronal subtypes,
367 including cholinergic neurons (using the *unc-17* promoter) and *gpa-14*-expressing
368 neurons. However, although both lines expressed the marker mNG in the expected
369 tissues, they also showed either recombination in unexpected cell types (for *unc-*
370 *17p::FLP*) or inefficient recombination (for *gpa-14p::FLP*) and were not characterized
371 in detail (Supplementary Figure S1B-C; see Discussion).

372 In the strains described above, co-expression of mNG serves to visualize when and
373 where FLP is expressed. However, in some experiments, the signal from mNG might
374 interfere with other fluorescent proteins. To circumvent this, we replaced mNG with
375 mTagBFP2 that emits blue light. When placed under control of the *hlh-12* promoter,
376 we observed mTagBFP2 expression and FLP-mediated recombination in both DTCs
377 of all animals (*n*=12; Supplementary Figure S1D). The sequences encoding mNG
378 and mTagBFP2 in the MosSCI plasmids are flanked by *Mlu*I restriction sites, which
379 facilitates the exchange of the former for the latter in the creation of new strains.

380

381 *Conditional gene knockout by GFP exon removal*

382 We previously designed a conditional knockout (KO) cassette based on GFP
383 containing FRT sites in introns 1 and 2 (Figure 2A) [20]. Excision of GFP exon 2 by
384 FLP causes a frame shift and a premature termination codon, which most likely
385 destabilizes the mRNA [61]. The premature termination codon precedes three short
386 open reading frames that are out of frame with respect to the gene downstream of
387 GFP. Together, this should completely prevent expression of the tagged protein. To
388 test this experimentally, we compared the consequence of either complete removal
389 of the *baf-1* gene (*gf>p::baf-1>*; "*>*" denotes the position of FRT; see Figure 2A) or
390 removal of GFP exon 2 in an endogenously tagged *gfp::baf-1* line (*g>f>p::baf-1*).
391 BAF-1 is an essential and ubiquitously expressed nuclear envelope protein [62]. In
392 both cases, we used the *nhx-2p::FLP* line described above to induce *baf-1* KO
393 specifically in intestinal cells, which negatively affects health [20]. As controls we
394 included (i) the *g>f>p::baf-1* line without FLP expression and (ii) an endogenously
395 tagged *mCh::baf-1* line without FRT sequences but with FLP expression. While
396 hermaphrodites of the two control lines produced an identical number of progeny
397 (*g>f>p::baf-1* 299±25 [mean±SD], n=10; *mCh::baf-1* 301±55, n=15), fertility was
398 reduced equally by 31% in the two conditional knockout lines (*g>f>p::baf-1; nhx-*
399 *2p::FLP* 207±71, n=15; *gf>p::baf-1>; nhx-2p::FLP* 206±68, n=12)(Figure 2B). Based
400 on this, we conclude that excision of the second exon of the GFP KO cassette
401 causes an equally strong loss of function phenotype as complete gene removal.
402 Moreover, it provides the advantage that insertion of the GFP KO cassette in the 5'-
403 end of a target gene in a single step is easier than inserting both a GFP tag (with a
404 single FRT) and a second FRT inside or downstream of the gene.

405 While conditional gene KO prevents synthesis of new transcripts, mRNA and protein
406 molecules already existing in the cell might persist for days, weeks or even months
407 [25]. This may obscure both investigation of gene function and potential therapeutic
408 interventions. To address this, we evaluated the kinetics of GFP::MEL-28 depletion
409 from hypodermal cells of *g>f>p::mel-28; dpy-7p::FLP* hermaphrodites. MEL-28 is a
410 component of the long-lived NUP107 nuclear pore subcomplex and is required for
411 DNA segregation and post-mitotic nuclear assembly [63,64,25]. Although the *dpy-7*
412 promoter is active already during embryogenesis to drive FLP expression, ~95% of
413 GFP::MEL-28 was still present in L1 larvae as compared to the control *g>f>p::mel-28*
414 line without FLP expression (Figure 3; compare Control and KO in 3B). In contrast, in
415 L2 larvae and young adults a dramatic reduction of the median GFP::MEL-28 signal
416 to ~12% and ~3%, respectively, was observed specifically in the hypodermis (Figure
417 3). This demonstrates the potential of conditional KO methods to evaluate the
418 function of long-lived proteins in late larvae and adults (see also below), whereas
419 they might be less suitable in early larvae.

FLP-mediated protein degradation

To enable analysis of long-lived proteins during development, we developed a system for FLP-mediated, inducible and rapid protein degradation from specific cells. A potent system for constitutive tissue-specific degradation of GFP-tagged proteins based on expression of vhhGFP4::ZIF-1, a GFP-binding nanobody fused to ZIF-1, was recently developed in *C. elegans* [3]. To achieve both temporal and spatial control of degradation of GFP-tagged proteins (hereafter termed GFPdeg), we replaced the *gfp::his-58* sequence of the dual color reporter with a sequence encoding vhhGFP4::ZIF-1. In this design, tissue-specificity is controlled by the choice of a particular FLP-expressing line, whereas temporal control is provided by the heat-inducible *hsp-16.41* promoter (Figure 4A).

We first determined that basal expression from the *hsp-16.41* promoter in the absence of heat induction does not cause depletion of GFP::MEL-28 in the hypodermis (Figure 4B). This implies that the system can be used to evaluate the function of essential proteins late in development by raising the animals at 16°C until induction. We next investigated whether the heat-induced GFPdeg system is equally efficient as the original constitutive variant [3]. We focused on degradation of GFP::MEL-28 in intestinal cells. GFP intensity was quantified in one or two intestinal cells closest to the pharynx and to the microscope lens to ensure consistent measurements. Other intestinal cells often lie below the gonad, impeding reproducible quantification. Three hours after a short heat pulse (15 min; 34°C) the median GFP::MEL-28 intensity was reduced to ~27% in the inducible GFPdeg strain, whereas slightly less protein remained in the constitutive GFPdeg strain (~18%; Figure 4C, left graph). By exposing the animals to two heat pulses, one 24h and another 3h prior to imaging, the efficiencies of the inducible and constitutive GFPdeg systems were equal (p=0.91; Figure 4C, right graph; Figure 4D). This demonstrates, that additional temporal control of the tissue-specific GFPdeg module can be achieved without compromising degradation efficiency. Depending on the protein of interest, induction conditions may have to be optimized. For instance, the efficiency of endogenous GFP::MEL-28 degradation in the intestine by either the constitutive or the inducible system (Figure 4C-D) is lower than the depletion reported for endogenous GFP::MDF-1 based on the identical constitutive GFPdeg strain [3]. To evaluate the degradation dynamics in more details, we measured GFP::MEL-28 levels in hypodermal cells at different time frames after a single induction of GFPdeg (15 min; 34°C). Hypodermis-specific expression of vhhGFP4::zif-1 was ensured by excision of *mCh::his-58* with FLP under the control of the *dpy-7* promoter. All images were taken from a region of the hypodermis closest to the lens and just posterior to the pharynx. One hour after induction, the median level of GFP::MEL-28 was reduced to ~55% and further down to ~19-20% after 2-4 h (Figure 5). A possible explanation for the remaining GFP::MEL-28 even at the optimal time points (2-4 h) could be novel protein synthesis since the degradation system will only be active for a finite time after induction. Indeed, substantial protein re-synthesis was observed 24 h after heat shock (Figure 5). The time frame of optimal degradation efficiency allows some flexibility in protocol design. However, these protocols, especially number and timing of heat inductions, presumably need to be tailored to the protein of interest and its turnover.

468 *Combination of FLP-mediated gene knockout and protein degradation*

469 Having available two FLP-controlled systems for inhibition of protein expression, we
470 decided to test the efficiency of combining them. In this setup, the same FLP driver
471 controls both conditional gene KO and protein degradation (Figure 6A). As a proof of
472 principle, we evaluated the combined action of the GFP KO cassette and GFPdeg on
473 the expression of endogenously GFP-tagged MEL-28 in the hypodermis.
474 Representative images of L1 and L2 larvae as well as young adults are shown in
475 Figure 6B whereas quantification is presented in Figure 3B. In contrast to the GFP
476 KO system which alone had insignificant effects in L1 larvae (Figure 3), the
477 combination of the two systems led to ~80% reduction of median GFP::MEL-28
478 signal. In L2 larvae, GFP::MEL-28 levels in the hypodermis were further decreased
479 to ~3% and undetectable in most young adults. Thus, in all three life stages tested,
480 the combination of conditional gene knockout and protein degradation provided the
481 most efficient inhibition of protein expression. We also compared the efficiency of
482 either conditional gene KO alone or in combination with targeted protein degradation
483 by inserting the GFP KO cassette in frame after the start codon of another stable
484 nuclear pore protein, NPP-2/NUP85. In young adults, the conditional KO caused a
485 reduction of ~97% of GFP::NPP-2 in the hypodermis, whereas only ~1.5% remained
486 when conditional KO was combined with the GFPdeg system (Figure 6C-D).

487 To test if these dramatic reductions of endogenous GFP::NPP-2 in the hypodermis
488 had consequences on the health of the animals, we determined their lifespan at
489 25°C. We followed >175 animals for each genotype and observed a 22-33%
490 reduction in median lifespan from 9 days post L4 in GFP::NPP-2 control animals
491 (95% confidence interval [CI] = 9-10 days) to 7 days in conditional KO animals (95%
492 CI = 6-7 days) and to 6 days in animals with combined conditional KO and GFPdeg
493 systems (95% CI = 6-7 days) (Figure 6E). Expression of FLP and GFPdeg in the
494 absence of the GFP KO cassette had no effect on the lifespan (p=0.3). The
495 statistically insignificant shift to the left of the lifespan curve for the animals with the
496 combined conditional KO and GFPdeg (red line) as compared to the animals with the
497 conditional KO only (dark red line; p=0.5) is in line with the unsubstantial (but
498 statistically significant) difference in GFP::NPP-2 signal intensity between the two
499 strains. We conclude that conditional NPP-2 KO in the hypodermis causes a
500 dramatic shortening of lifespan, illustrating the suitability of the combination of the
501 GFP KO cassette and the GFPdeg system for evaluation of physiological
502 consequences of protein depletion in specific tissues.

503

504 *Tissue-specific profiling of nascent mRNA transcription by SLAM-ITseq*

505 Various methods are available for analysis of gene expression profiles in specific cell
506 types in *C. elegans*, including physical isolation of cells or nuclei of interest [65-67],
507 affinity purification of RNAs from specific cells [68], trans-splicing-based RNA tagging
508 [69], and mapping of RNA polymerase occupancy [14,70]. While each of these
509 methods present advantages and limitations, none of them allows the specific
510 identification of nascent transcripts at a particular time point during development.
511 Recently, Matsushima and co-workers reported an *in vivo* labeling technique in
512 mouse that enables tissue-specific profiling of nascent mRNAs without cell sorting
513 [30]. The method is based on thiol(SH)-linked alkylation for the metabolic sequencing
514 of RNA in tissue (SLAM-ITseq) and relies on expression of the enzyme uracil
515 phosphoribosyltransferase (UPRT) from the protozoan *Toxoplasma gondii* in specific

516 cell types. UPRT encoded by the genomes of most multicellular organisms, including
517 *C. elegans*, lacks two amino acid residues involved in uracil binding and show no
518 UPRTase activity *in vitro* [71]. By providing 4-thiouracil (4-TU) at a given moment to
519 animals that express *T. gondii* UPRT in a specific tissue, 4-TU will be converted to 4-
520 thiouridine monophosphate (4-thio-UMP) in a spatiotemporal manner [30]. RNA
521 polymerases incorporate 4-thio-UMP during transcription to generate thiol-containing
522 RNA (thio-RNA), which subsequently is identified by alkylation and deep sequencing
523 (Figure 7A).

524 To adapt SLAM-ITseq for *C. elegans*, we inserted a codon-optimized version of the
525 *T. gondii* UPRT gene downstream of the FRT-flanked *mCh::his-58* cassette and
526 under control of the strong and ubiquitous *eft-3* (*eef-1A.1*) promoter (Figure 7A). We
527 introduced a single copy of this construct into the *C. elegans* genome and crossed
528 the resulting line with various FLP drivers. FLP-dependent expression of UPRT was
529 confirmed by Western blotting (Supplementary Figure S2A). As a proof of concept,
530 we exposed animals that express UPRT in the hypodermis using a *dpy-7p::FLP*
531 driver to 4-TU from L3 to L4 stage and purified total RNA. RNA from animals without
532 FLP expression was used to control for UPRT-independent labeling. RNA was
533 alkylated with iodoacetamide, which leads to a T>C conversion of 4-TU-labeled
534 positions during cDNA synthesis [72], and subjected to deep sequencing (see
535 Materials and Methods). We first tested if the presence of FLP and UPRT affected
536 gene expression, and concluded that this was not the case (Supplementary Figure
537 S2B-D). Comparing the T>C conversion rate per gene revealed a significant
538 increase in nematodes expressing UPRT in the hypodermis (Figure 7B). Next, we
539 performed a beta-binominal test to identify genes that were significantly labelled
540 across all replicas [30], which retrieved 197 genes ($p<0.003$; FDR<0.1 after
541 adjustment for multiple comparisons; Figure 7C; Supplementary Table S5). To
542 illustrate the reproducibility of the method, T>C fractions of 4 genes reported to be
543 expressed in the hypodermis are shown (*pars-1*, *mig-15*, *dpy-3* and *nhr-97*;
544 FDR<0.03; Figure 7D). Finally, to evaluate the specificity of SLAM-ITseq, we
545 compared the list of 197 nascent transcripts to three datasets of genes reported to
546 be expressed in the hypodermis [70,67,68] (Figure 7E). Our list overlapped
547 significantly with all three datasets (168/197 = 85%; $p<1e-10$ Fisher's exact test),
548 which represents the second highest overlap. Moreover, of the 29 genes not
549 overlapping with any of the three other datasets, at least 20 (69%) are reliably
550 detected in hypodermal cells in single cell RNAseq performed on embryos [73] or L2
551 larvae [74]. We conclude that SLAM-ITseq is an attractive and easily applicable
552 method to identify nascent transcripts with high confidence. We expect that the
553 method can be further optimized to increase the T>C fractions and thereby increase
554 the sensitivity.

555

556 **Discussion**

557 An increasing number of specific and efficient FLP and Cre drivers generated by the
558 *C. elegans* community are facilitating a variety of precise functional assays to
559 interrogate neural circuits [10,13,24,12], cell proliferation and differentiation [11],
560 gene expression programs [14,51] and chromatin organization [15,16]. In this study,
561 we report four new FLP lines that reliably induce recombination specifically in either
562 distal tip cells, the somatic gonad, coelomocytes or in epithelial Pn.p cells. The
563 efficiency of recombination was ~100% in all animals evaluated for the four lines. In

564 the case of the *ckb-3p::FLP* line, recombination was observed already in the earliest
565 progenitors Z1 and Z4, which implies that the line is suitable to target all cell types of
566 the somatic gonad, including distal tip cells, gonadal sheath, spermatheca,
567 spermatheca-uterine valve and the uterus [53]. In contrast, the activity of the *hlh-*
568 *12p::FLP* line is restricted to the distal tip cell and may thus be useful to investigate
569 its stem cell niche function [75]. Similarly, biological processes in coelomocytes are
570 amenable to manipulation by the *unc-122p::FLP* line, whereas the *lin-31p::FLP* line
571 induces recombination in the cells producing the vulva. We previously created a FLP
572 line to induce recombination in intestinal cells based on the *elt-2* promoter. However,
573 because this promoter can also drive expression in other tissues [20,11], we
574 developed here a novel line based on the *nhx-2* promoter. The new line is equally
575 efficient to produce recombination in the intestine (Table 1) and with the advantage
576 of not provoking recombination elsewhere. We also attempted to construct lines for
577 specific neurons using the promoters of *gpa-14* and *unc-17*. In the case of *gpa-14*,
578 we observed variable recombination rates in FLP-expressing cells (0, 1 or 2 alleles
579 of the single-copy reporter). It seems that the behavior of the specific cells is
580 reproducible between individuals, but we do not know if this is due to differences in
581 FLP expression levels and/or the FRT sites being less accessible in certain cells. For
582 the *unc-17p::FLP* line, we observed widespread recombination in cholinergic
583 neurons as expected but also in the hypodermis. We speculate that this could be
584 due to an inability of our construct to precisely reflect *unc-17* expression [76],
585 although we also note that two cholinergic neurons, PVNL and PVNR, are sister cells
586 to two hypodermal cells (TLappa and TRappa). Thus, if *unc-17p::FLP* is activated
587 already in the progenitor cells TLapp and TRapp, GFP::HIS-58 expression would be
588 expected in both cell types.

589 We previously proposed that inserting a GFP KO cassette (with FRT sites in *gfp*
590 introns 1 and 2) immediately after the start codon of a gene provides an informative
591 GFP fusion protein and a conditional KO allele in a single step [20]. In this study we
592 have further validated this approach by comparing strains that either carry the GFP
593 KO cassette in the endogenous *baf-1* locus or a GFP cassette with a single FRT and
594 a second FRT downstream of *baf-1*. When combined with an *nhx-2p::FLP* driver to
595 KO *baf-1* specifically in the intestine, identical reductions of fertility were detected in
596 the two strains. Furthermore, using the GFP KO cassette, we determined that
597 conditional KO of *npp-2*/NUP85 in the hypodermis caused a dramatic lifespan
598 shortening. We therefore conclude that insertion of the GFP KO cassette into an
599 endogenous locus by CRISPR provides an attractive dual tool to study protein
600 dynamics and KO phenotypes in a single workflow.

601 Although gene KO is often considered an ultimate test for gene function, slow mRNA
602 and protein turnover can delay the appearance of loss-of-function phenotypes. This
603 is particularly relevant for organisms with rapid development and relatively short
604 lifespan, such as *C. elegans*. Targeted protein degradation is a relevant alternative
605 and auxin-inducible degradation (AID) stands out as an attractive and popular option
606 due to its fast kinetics and both inducible and reversible nature [2]. Concerns have
607 been raised regarding auxin-independent depletion of AID-tagged proteins (see
608 references in [6]) and potential effects of auxin on endoplasmic reticulum stress [77],
609 but recent optimization of AID tools may have overcome this [4]. We show here that
610 GFPdeg, an alternative protein degradation system based on a GFP-binding
611 nanobody [3] and adapted for FLP-mediated spatiotemporal control, can efficiently
612 deplete 80% of a long-lived nuclear pore protein, MEL-28/ELYS, fused to GFP. By

comparing the degradation of GFP::MEL-28 in intestinal cells using either the original, constitutive version of GFPdeg [3] or the heat inducible version of GFPdeg developed in this study, we conclude that they are equally efficient. Importantly, the GFPdeg system is immediately applicable to study the function of any GFP-tagged fusion protein. We chose to focus on stable nuclear pore proteins [26,25] in our study as they are probably more challenging to deplete but we assume that higher depletion efficiencies will be observed for proteins with shorter half-lives. The original GFPdeg version [3] has the advantage that it involves only two components (GFP-tagged fusion protein and constitutive, tissue-specific GFPdeg) and does not require induction. In contrast, our FLP-based GFPdeg system includes three components (GFP-tagged fusion protein, tissue-specific FLP driver and heat-inducible, FRT-flanked GFPdeg) and requires one or two short 15 min exposures to 34°C. On the other hand, our inducible system allows to evaluate processes at any stage in development or during aging by raising the nematodes at standard temperatures until induction at the desired time point. This cannot be achieved with the constitutive system where the animal's development potentially arrests once the concentration of the target protein is below a required threshold. We envision that the FLP-controlled GFPdeg system can be further modified to incorporate other inducers [78,79,5] in situations where short heat pulses are incompatible with the experimental design.

Depending on the experimental setup, either site-specific gene KO or targeted protein degradation may be sufficient to elucidate gene function. However, bimodal control of protein levels may be particularly valuable for the study of long-lived proteins during early developmental stages as highlighted in this study. By combining the GFP KO cassette and the GFPdeg system, we have generated a protocol that provides two-fold control of tissue-specific protein depletion. On one hand, a specific FLP driver induces gene KO in a tissue of interest and thus prevents synthesis of mRNA from the target gene. On the other hand, the same FLP driver excises tissue-specifically the FRT-flanked *mCh::his-58* cassette from the GFPdeg construct, thus enabling heat-induced and rapid degradation of existing GFP-tagged target protein. We show that the combined KO and GFPdeg systems can deplete GFP::MEL-28 and GFP::NPP-2 to non-detectable levels, thus offering a highly efficient approach for spatiotemporal control of protein levels in a multicellular organism.

One of the strengths of recombinase-based genome engineering is its versatility: the possibility of using collections of stable FLP and Cre drivers to control a variety of different effectors through straight-forward genetic crosses [7,6,5]. In this study we have widened the range of applications for transcriptomic profiling by introducing SLAM-ITseq for *C. elegans*. Cre/loxP was recently utilized to generate tissue-specific transcription footprints by RNA pol DamID (RAPID) [14]. The two methods are complementary with RAPID providing cumulative information on genes expressed throughout the life of the cell whereas SLAM-ITseq is designed for identification of nascent transcripts [30]. We have demonstrated the potential of SLAM-ITseq in *C. elegans* by expressing UPRT specifically in the hypodermis through the use of a *dpy-7p::FLP* driver and identified 197 genes. We could not compare our list from SLAM-ITseq to the RAPID method because different tissues were analyzed. Instead, we compared our list with hypodermal data from another recent DamID-based (TaDa) study [70] and found a significant overlap ($p=1.6e-11$). We also found significant overlaps when comparing our data with hypodermal lists from two other methods, PATseq [68] and FACS [67] ($p<2.2e-16$). We consider it relevant to note

662 that the percentage of genes found uniquely in SLAM-ITseq (i.e. not confirmed by
663 any of the three other methods) is quite low (15% vs. 19-30% for PATseq and
664 FACS). Moreover, most (20/29) of the genes in this category have been detected in
665 cells classified as hypodermal cells in single-cell RNAseq studies [74,73]. We
666 therefore conclude that genes identified by SLAM-ITseq can be considered high-
667 confidence hits.

668 The number of genes in our SLAM-ITseq hypodermal list is >10-fold lower than the
669 lists from the three other methods. We propose three explanations that are not
670 mutually exclusive. Firstly, SLAM-ITseq will only capture mRNAs synthesized during
671 the interval from when 4-thio-UMP becomes available in the cells until harvest of the
672 sample. In this proof-of-concept study, nematodes were incubated with 4-TU for 17h
673 from L3 to L4 stage but the kinetics of 4-TU uptake and conversion to 4-thio-UMP by
674 UPRT are unknown. Thus, the effective labeling time might be considerably shorter.
675 The other methods discussed here provide either the history of transcription during
676 the life of the cell (RAPID and TaDa) or a compilation of all mRNAs present in the
677 cell at the time of harvest (PATseq and FACS). Depending on the biological question
678 that needs to be addressed, a particular method might be most suitable. Secondly,
679 the two methods that report the largest gene sets have higher intrinsic risks of
680 including false positive hits. For instance, FACS isolation of a particular cell type
681 might include contaminants in the form of cells from other tissues. Similarly, in the
682 PATseq protocol, mRNA from unlabeled cells might potentially co-purify with the
683 mRNA from the target cells. Such false positives are difficult to control for in the
684 FACS and PATseq protocols. In contrast, the SLAM-ITseq method is based on
685 isolation and sequencing of total mRNA followed by a statistical analysis to identify
686 transcripts with a higher labelling ratio in the UPRT expressing cells. Thirdly, we
687 speculate that conversion of 4-TU to 4-thio-UMP in *E. coli* used as food for the
688 nematodes during the experiment might cause a relative high background labeling
689 [80,81]. The median ratio of T>C conversions in control mice without UPRT in the
690 original SLAM-ITseq study [30] was ~2 fold lower (~0.03%) than our observation in
691 the *C. elegans* control strain without UPRT expression (- FLP; 0.07%). In contrast,
692 the median T>C ratio in the *C. elegans* strain with UPRT expression (+ FLP; 0.10%)
693 was similar to the ratio in endothelial cells expressing UPRT in the mouse brain
694 (~0.10%). Considering that hypodermal nuclei constitute approximately 12% of the
695 total nuclei in L4 larvae (somatic and germ line) and assuming that background
696 labelling is uniform across tissues, we estimate that the UPRT-specific labelling is
697 ~3.5 folder higher than the background labelling. The higher frequency of UPRT-
698 independent T>C conversions in our *C. elegans* sample implies that fewer genes
699 appear as significantly labeled in the strain with UPRT expression. Indeed, we even
700 identified 13 genes with higher T>C conversions in the strain without UPRT
701 expression. This is much fewer than the 197 hits identified in the strain with UPRT
702 expression, but it nevertheless calls for future studies to improve the sensitivity of
703 SLAM-ITseq in *C. elegans*. We propose to investigate the influence of *E. coli*
704 nucleotide metabolism, for instance by using dead bacteria as food source. In any
705 case, we conclude that SLAM-ITseq has the capacity to identify nascent transcripts
706 in a tissue of interest with high confidence. We have tested the method in the
707 hypodermis, but it is easily applied to other cell types for which an appropriate FLP
708 driver is available. In particular, we envision that SLAM-ITseq will be advantageous
709 for cell types that are hard to isolate in an intact state, such as neurons.

710

711 **Table 1 Efficiency of FLP-mediated recombination**

Promoter	Cell type	Stage[a]	Observed[b]	Expected	Efficiency
ckb-3	Somatic gonad	Early L1	2.0±0.2 (36)	2	99%
hlh-12	Distal tip cell	L2-adult	2.0±0.0 (24)	2	100%
lin-31	P1.p-P11.p (P5.p-P7p)	L2-L4	3.0±0.0 (14)	3[c]	100%
		L3	12.0±0.0 (13)	12[c]	100%
		L4	22.0±0.0 (3)	22[c]	100%
nhx-2	Intestine	L1	20.0±0.0 (10)	20 (19-22)	100%
		L2	31.9±0.6 (17)	32 (19-22)	100%
unc-122	Coelomocytes	L1	4.0±0.0 (8)	4	100%
		L3-L4	6.0±0.0 (23)	6	100%

712 [a] Developmental stage that was used for determination of recombination efficiency.

713 [b] Average number of GFP positive nuclei ± SD; number in brackets: *n*.

714 [c] Efficiencies were calculated based on recombination in central Pn.p cells and their
715 descendants.

716

717 **Acknowledgments**

718 We are grateful to Andrew Chisholm, Carmen Ortiz González, Fernando Monje-
719 Casas, Michael Krieg, Montserrat Porta, Ngang Heok Tang, Patricia Regina Rider
720 García and Wayo Matsushima for reagents and advice and Raquel Romero-Bueno
721 for critical reading of the manuscript. We also wish to acknowledge Ana Miñan
722 Fernández from the CABD Functional Genomics Facility for microinjections, Laura
723 Tomás from the CABD Proteomics and Biochemistry Facility for recombinant
724 proteins, Katherina García from the CABD Imaging Facility for technical assistance;
725 the Caenorhabditis Genetics Center (CGC), which is funded by the National
726 Institutes of Health (NIH) Office of Research Infrastructure Programs (P40
727 OD010440) and WormBase. This project was funded by the Spanish State Research
728 Agency and the European Regional Development Fund (BFU2016-79313-P, MDM-
729 2016-0687 and PID2019-105069GB-I00).

730

731 **Figure legends**

732 Figure 1. Characterization of novel FLP lines. (A) Schematic representation of the
733 dual color reporter used to evaluate recombination activity. Upon temperature
734 induction of the *hsp-16.41* promoter, the reporter expresses red (mCh) or green

735 (GFP) histone HIS-58 in cell lineages without or with FLP-mediated recombination,
736 respectively. (B) Evaluation of FLP lines crossed with the dual color reporter.
737 Although the FLP lines co-express diffuse mNG in the cytoplasm, GFP::HIS-58 is
738 clearly visible in the expected nuclei. (Ba) *ckb-3p::FLP::SL2::mNG*: maximum
739 projections of 2-3 confocal sections of BN854 L1 larva (Ba') and larva at L3/L4 molt
740 (Ba''). The Z1 and Z4 somatic gonad precursor cells are indicated. (Bb) *hlh-*
741 *12p::FLP::SL2::mNG*: single confocal sections of BN1204 L2 larva (Bb') and young
742 adult (Bb''). The distal tip cells (DTCs) are indicated. (Bc) *lin-31p::FLP::SL2::mNG*:
743 maximum projections of three confocal sections of BN1023 L2 larva (Bc') and L4
744 larva (Bc''). The posterior daughters of P1-P7 and vulA-vulF forming the vulva are
745 indicated. (Bd) *nhx-2p::FLP::SL2::mNG*: maximum projection of five confocal
746 sections of BN999 L1 larva (Bd'; indicated area shown enlarged in Bd''). (Be) *unc-*
747 *122p::FLP::SL2::mNG*: maximum projections of four confocal sections of BN1029 L1
748 larva (Be') and L4 larva (Be''). The three pairs of coelomocytes are indicated. Scale
749 bars 10 µm.

750 Figure 2. Comparison of GFP KO cassette and complete gene KO. (A) Schematic
751 representation of the two KO strategies. In the first strategy (top), a GFP KO
752 cassette with FRTs in *gfp* introns 1 and 2 is inserted upstream of, and in frame with,
753 a gene of interest (here *baf-1*). FLP-mediated recombination leads to a frame shift
754 and a premature termination codon ("Stop"). In case the ribosome remains
755 associated with the mRNA, the three downstream open reading frames are all out-of-
756 frame with *baf-1* (purple lines). In the second strategy (bottom), the GFP cassette
757 contains a single FRT and a second FRT is inserted in the 3'-UTR of the gene of
758 interest. FLP-mediated recombination leads to complete gene removal. (B) Brood
759 sizes were determined for control animals (*g>f>p::baf-1* and *mCh::baf-1; nhx-*
760 *2p::FLP*) and for animals with conditional KO of *baf-1* in the intestine (*g>f>p::baf-1;*
761 *nhx-2p::FLP* [first strategy] and *gf>p::baf-1>; nhx-2p::FLP* [second strategy]; strains
762 BN580, BN1182 and BN1223). Each point represents the number of progenies
763 produced by an individual worm; *n* for each genotype is indicated in parenthesis. P
764 values from Wilcoxon rank sum tests and adjusted for multiple comparisons
765 (Benjamini & Hochberg method) are indicated. In these and subsequent boxplots,
766 the midline represents the median and the upper and lower limits of the box
767 correspond to the third and first quartile, respectively. The whiskers extend to the
768 lowest and higher observations but maximum up to 1.5 times the interquartile range.

769 Figure 3. KO of GFP::MEL-28 in hypodermal nuclei. (A) Confocal micrographs of
770 *g>f>p::mel-28* L1 larvae, L2 larvae and young adults either not expressing FLP (top
771 panels; strain BN793) or expressing FLP in the hypodermis (bottom panels; *dpy-*
772 *7p::FLP* driver; strain BN1121). A single focal plane of the hypodermis is shown.
773 Scale bar 10 µm. (B) Quantification of GFP::MEL-28 at the nuclear envelope of
774 hypodermal nuclei. Each point represents a single nucleus. Data were acquired from
775 at least 10 animals in two independent experiments; *n* for each genotype is indicated
776 in parenthesis. P values from Wilcoxon rank sum tests and adjusted for multiple
777 comparisons (Benjamini & Hochberg method) are indicated. Examples of Control
778 (strain BN793) and KO (strain BN1121) animals are shown in (A); examples of
779 combined KO + GFPdeg are in Figure 6B (strain BN1122).

780 Figure 4. Degradation of GFP::MEL-28 in intestinal cells. (A) Schematic
781 representation of the GFPdeg strategy. The vhhGFP4::ZIF-1 fusion protein targets
782 GFP-tagged proteins for rapid degradation. Temporal and spatial control is provided
783 by the *hsp-16.41* promoter and tissue-specific FLP expression, respectively. (B)

784 Quantification of GFP::MEL-28 at the nuclear envelope of hypodermal nuclei of
785 young adults either without the GFPdeg system (Control; strain BN452) or with the
786 GFPdeg system but without induction (GFPdeg; strain BN1084). (C) Quantification of
787 GFP::MEL-28 at the nuclear envelope of anterior intestinal nuclei of young adults
788 after 1 or 2 rounds of GFPdeg induction in the intestine (*nhx-2p::FLP* driver; strain
789 BN1118). Control (strain BN452) and constitutive degradation (*elt-2p::vhhGFP4::zif-*
790 *1*; strain BN746) are included for comparison. Graph details are explained in Figure
791 3. (D) Confocal micrographs of *gfp::mel-28* young adults without GFPdeg (top
792 panels; strain BN452), inducible intestinal GFPdeg (middle panels; strain BN1118) or
793 constitutive intestinal GFPdeg (bottom panels; strain BN746). A single focal plane of
794 the anterior pair of intestinal nuclei is shown. Scale bar 10 µm.

795 Figure 5. Kinetics of GFP::MEL-28 degradation in hypodermal cells. (A) Confocal
796 micrographs of *gfp::mel-28* young adults either without induction or 1-24 h after
797 induction of GFPdeg in the hypodermis (*dpy-7p::FLP* driver; strain BN1084). A single
798 focal plane of the hypodermis is shown. Scale bar 10 µm. (B) Quantification of
799 GFP::MEL-28 at the nuclear envelope of hypodermal nuclei. Graph details are
800 explained in Figure 3.

801 Figure 6. Efficient protein depletion by combined gene KO and GFPdeg. (A)
802 Schematic representation of the combined KO and GFPdeg strategy. A single FLP
803 driver controls tissue-specifically both KO (left) and protein degradation (right) of a
804 gene tagged with the GFP KO cassette. (B) Confocal micrographs of *g>f>p::mel-28*
805 L1 larvae, L2 larvae and young adults either not expressing FLP (top panels; strain
806 BN793) or expressing FLP and GFPdeg in the hypodermis (bottom panels; *dpy-*
807 *7p::FLP* driver; strain BN1122). A single focal plane of the hypodermis is shown.
808 Scale bar 10 µm. Quantification is shown in Figure 3B. (C) Confocal micrographs of
809 *g>f>p::npp-2* L4 larvae either not expressing FLP (left panel; strain BN1082),
810 expressing FLP in the hypodermis (middle panel; *dpy-7p::FLP* driver; strain BN1111)
811 or expressing FLP and vhhGFP4::ZIF-1 in the hypodermis (right panel; *dpy-7p::FLP*
812 driver; strain BN1086). A single focal plane of the hypodermis is shown. Scale bar 10
813 µm. (D) Quantification of GFP::NPP-2 at the nuclear envelope of hypodermal nuclei.
814 Graph details are explained in Figure 3. (E) Survival curves for animals expressing
815 GFP::NPP-2 alone (blue; strain BN1082) or combined with either FLP in the
816 hypodermis (dark red; strain BN1111) or FLP and GFPdeg in the hypodermis (red;
817 strain BN1086). A strain with hypodermal FLP and GFPdeg but without target was
818 included as control (green; BN1097). The lifespan of the two strains with depletion of
819 GFP::NPP-2 in the hypodermis was significantly shorter compared to the two control
820 strains (*** indicates p<1e-08). More than 175 animals were analysed for each
821 genotype.

822 Figure 7. Tissue-specific identification of nascent transcripts by SLAM-ITseq. (A)
823 Schematic representation of the SLAM-ITseq method. Temporal and spatial control
824 is provided by exposure to 4-thio-uracil and tissue-specific FLP expression,
825 respectively. In tissues that express UPRT, 4-thio-uracil is converted to 4-thio-UMP,
826 which is incorporated into nascent transcripts by RNA polymerases. After
827 purification, the total RNA is treated with an alkylating reagent, which leads to T>C
828 conversion during cDNA synthesis. (B-E) Data based on four replicas of control L4s
829 not expressing FLP (- FLP; strain BN1158) and three replicas of L4s expressing FLP
830 in the hypodermis (+ FLP; *dpy-7p::FLP* driver; strain BN1190). The analysis was
831 restricted to 20,767 poly-adenylated transcripts with at least one read in all replicas
832 (*CoverageOnTs* > 0). (B) Distribution of T>C conversion rates for all 20,767

833 transcripts. (C) Representation of T>C conversion rates for individual transcripts.
834 Red points indicate 197 genes with a significantly higher T>C conversion rate in +
835 FLP animals (FDR<0.1). Blue points mark *unc-54* and *glh-2* which both appear as
836 significantly enriched. This is expected, because the *unc-54* and *glh-2* 3'-UTRs are
837 used in the UPRT and FLP transgenes, respectively. Black points indicate 13 genes
838 with a statistically higher T>C conversion rate in - FLP animals (FDR<0.1). (D)
839 Examples of T>C conversion rates for individual genes and individual replicas. Lines
840 represent the means. (E) Comparison of the 197 nascent transcripts identified by
841 SLAM-ITseq with three alternative methods for transcriptomic profiling (see main text
842 for details). Numbers in parentheses indicate the number of genes reported in each
843 study; percentages in parentheses indicate the fraction of genes reported uniquely in
844 each study.

845 Supplementary Figure S1. Characterization of novel FLP drivers. Upon temperature
846 induction of the *hsp-16.41* promoter, the reporter expresses red (mCh) or green
847 (GFP) histone HIS-58 in cell lineages without or with FLP-mediated recombination,
848 respectively. (A) Recombination activity by *lin-31p::FLP::SL2::mNG* is observed in
849 the head (left panel) and central region (right panel) of BN1023 animals. Bright
850 GFP::HIS-58 expression is observed in the nuclei of cells forming the vulva (filled
851 arrows), whereas faint expression is detected in the hypodermis (open arrows; right
852 panel). Presumably, the faint expression is derived from Pn.p cells that fuse with
853 hyp7. (B) Recombination activity by *gpa-14p::FLP::SL2::mNG* is observed in the
854 head (left panel) and tail (right panel) of BN1208 animals. Filled arrows point to
855 nuclei expressing GFP::HIS-58 but not mCh::HIS-58 (i.e. recombination of both
856 alleles); a double arrow points to a nucleus expressing both fluorescent proteins (i.e.
857 recombination of one allele) and open arrows indicate cells that express diffuse mNG
858 (and hence also FLP) but not GFP::HIS-58. (C) Expression of mNG from the *unc-*
859 *17p::FLP::SL2::mNG* transgene overlaps with mKate2 signal from endogenously
860 tagged *unc-17* (lower left panel) and recombination (GFP::HIS-58) is detected as
861 expected in multiple neurons in the head (upper left panel) and ventral nerve cord
862 (upper right panel) of BN1133 animals. Unexpectedly, GFP::HIS-58 is also observed
863 in hypodermal nuclei (lower right panel). (D) Recombination activity by *hlh-*
864 *12p::FLP::SL2::mTagBFP2* is observed in the distal tip cell of BN1319 animals. The
865 distal tip cell is marked by co-expressed mTagBFP2. Scale bars 10 µm.

866 Supplementary Figure S2. Evaluation of UPRT expression and its effect on gene
867 expression. (A) Protein extracts from nematodes not expressing FLP (- FLP; strain
868 BN1158) or expressing FLP in the hypodermis (+ FLP; strain BN1190) were
869 analyzed by gel electrophoresis followed by protein visualization (left) or Western
870 blotting and probing with anti-HA antibodies (right). A band of the expected size is
871 observed specifically in the + FLP sample. (B) Spearman correlation coefficients for
872 pairwise comparisons of reads per transcript (*CoverageOnTs*) in four - FLP
873 (BN1158) and three + FLP (BN1190) samples. All values are >0.90. (C) Scatter plot
874 of reads per transcript in - FLP (average of 4 samples) versus + FLP (average of 3
875 samples). (D) Graphic representation of DESeq2 analysis of data from panel C
876 (restricted to 20,767 poly-adenylated transcripts with CoverageOnTs > 0 in all
877 replicas). All data points are displayed in grey, implying no statistically difference
878 between the two genotypes (FDR<0.1). Based on the results in panels B-D, we
879 conclude that expression of FLP and UPRT in the hypodermis does not alter gene
880 expression.

881

882 **References**

883 1. Watts JS, Harrison HF, Omi S, Guenthers Q, Dalelio J, Pujol N, Watts JL (2020)
884 New Strains for Tissue-Specific RNAi Studies in Caenorhabditis elegans. G3
885 (Bethesda) 10 (11):4167-4176. doi:10.1534/g3.120.401749
886 2. Zhang L, Ward JD, Cheng Z, Dernburg AF (2015) The auxin-inducible degradation
887 (AID) system enables versatile conditional protein depletion in C. elegans.
888 Development 142 (24):4374-4384. doi:10.1242/dev.129635
889 3. Wang S, Tang NH, Lara-Gonzalez P, Zhao Z, Cheerambathur DK, Prevo B,
890 Chisholm AD, Desai A, Oegema K (2017) A toolkit for GFP-mediated tissue-specific
891 protein degradation in C. elegans. Development 144 (14):2694-2701.
892 doi:10.1242/dev.150094
893 4. Hills-Muckey K, Martinez MAQ, Stec N, Hebbar S, Saldanha J, Medwig-Kinney
894 TN, Moore FEQ, Ivanova M, Morao A, Ward JD, Moss EG, Ercan S, Zinovyeva AY,
895 Matus DQ, Hammell CM (2021) An engineered, orthogonal auxin
896 analog/AtTIR1(F79G) pairing improves both specificity and efficacy of the auxin
897 degradation system in Caenorhabditis elegans. Genetics.
898 doi:10.1093/genetics/iyab174
899 5. Driesschaert B, Mergan L, Temmerman L (2021) Conditional gene expression in
900 invertebrate animal models. J Genet Genomics 48 (1):14-31.
901 doi:10.1016/j.jgg.2021.01.005
902 6. Nance J, Frokjaer-Jensen C (2019) The Caenorhabditis elegans Transgenic
903 Toolbox. Genetics 212 (4):959-990. doi:10.1534/genetics.119.301506
904 7. Hubbard EJ (2014) FLP/FRT and Cre/lox recombination technology in C. elegans.
905 Methods 68 (3):417-424. doi:10.1016/j.ymeth.2014.05.007
906 8. Sauer B (1987) Functional expression of the cre-lox site-specific recombination
907 system in the yeast Saccharomyces cerevisiae. Mol Cell Biol 7 (6):2087-2096.
908 doi:10.1128/mcb.7.6.2087-2096.1987
909 9. Senecoff JF, Bruckner RC, Cox MM (1985) The FLP recombinase of the yeast 2-
910 micron plasmid: characterization of its recombination site. Proc Natl Acad Sci U S A
911 82 (21):7270-7274. doi:10.1073/pnas.82.21.7270
912 10. Konietzka J, Fritz M, Spiri S, McWhirter R, Leha A, Palumbos S, Costa WS,
913 Oranth A, Gottschalk A, Miller DM, 3rd, Hajnal A, Bringmann H (2020) Epidermal
914 Growth Factor Signaling Promotes Sleep through a Combined Series and Parallel
915 Neural Circuit. Curr Biol 30 (1):1-16 e13. doi:10.1016/j.cub.2019.10.048
916 11. Ruijtenberg S, van den Heuvel S (2015) G1/S Inhibitors and the SWI/SNF
917 Complex Control Cell-Cycle Exit during Muscle Differentiation. Cell 162 (2):300-313.
918 doi:10.1016/j.cell.2015.06.013
919 12. Schmitt C, Schultheis C, Pokala N, Husson SJ, Liewald JF, Bargmann CI,
920 Gottschalk A (2012) Specific expression of channelrhodopsin-2 in single neurons of
921 Caenorhabditis elegans. PLoS One 7 (8):e43164. doi:10.1371/journal.pone.0043164
922 13. Davis MW, Morton JJ, Carroll D, Jorgensen EM (2008) Gene activation using
923 FLP recombinase in C. elegans. PLoS Genet 4 (3):e1000028.
924 doi:10.1371/journal.pgen.1000028
925 14. Gomez-Saldivar G, Osuna-Luque J, Semple JI, Glauser DA, Jarriault S, Meister
926 P (2020) Tissue-Specific Transcription Footprinting Using RNA Pol DamID (RAPID)
927 in Caenorhabditis elegans. Genetics. doi:10.1534/genetics.120.303774
928 15. Cabianca DS, Munoz-Jimenez C, Kalck V, Gaidatzis D, Padeken J, Seeber A,
929 Askjaer P, Gasser SM (2019) Active chromatin marks drive spatial sequestration of
930 heterochromatin in C. elegans nuclei. Nature 569 (7758):734-739.
931 doi:10.1038/s41586-019-1243-y

16. Harr JC, Schmid CD, Munoz-Jimenez C, Romero-Bueno R, Kalck V, Gonzalez-Sandoval A, Hauer MH, Padeken J, Askjaer P, Mattout A, Gasser SM (2020) Loss of an H3K9me anchor rescues laminopathy-linked changes in nuclear organization and muscle function in an Emery-Dreifuss muscular dystrophy model. Genes Dev. doi:10.1101/gad.332213.119
17. Nonet ML (2020) Efficient Transgenesis in Caenorhabditis elegans Using Flp Recombinase-Mediated Cassette Exchange. Genetics 215 (4):903-921. doi:10.1534/genetics.120.303388
18. Ge MH, Wang W, Wu TH, Wen X, Al-Sheikh U, Chen LL, Yin SW, Wu JJ, Huang JH, He QQ, Liu H, Li R, Wang PZ, Wu ZX (2020) Dual Recombining-out System for Spatiotemporal Gene Expression in C. elegans. iScience 23 (10):101567. doi:10.1016/j.isci.2020.101567
19. Kage-Nakadai E, Imae R, Suehiro Y, Yoshina S, Hori S, Mitani S (2014) A conditional knockout toolkit for Caenorhabditis elegans based on the Cre/loxP recombination. PLoS One 9 (12):e114680. doi:10.1371/journal.pone.0114680
20. Munoz-Jimenez C, Ayuso C, Dobrzynska A, Torres-Mendez A, Ruiz PC, Askjaer P (2017) An Efficient FLP-Based Toolkit for Spatiotemporal Control of Gene Expression in Caenorhabditis elegans. Genetics 206 (4):1763-1778. doi:10.1534/genetics.117.201012
21. Voutev R, Hubbard EJ (2008) A "FLP-Out" system for controlled gene expression in Caenorhabditis elegans. Genetics 180 (1):103-119. doi:10.1534/genetics.108.090274
22. Macias-Leon J, Askjaer P (2018) Efficient FLP-mediated germ-line recombination in C. elegans. MicroPubl Biol 2018. doi:10.17912/W2G66S
23. Ayuso C, Askjaer P (2019) Spatiotemporal control of genome recombination through combined FLP-Frt and GAL4-UAS technologies. MicroPubl Biol 2019. doi:10.17912/micropub.biology.000089
24. Davis L, Radman I, Goutou A, Tynan A, Baxter K, Xi Z, O'Shea JM, Chin JW, Greiss S (2021) Precise optical control of gene expression in C elegans using improved genetic code expansion and Cre recombinase. Elife 10. doi:10.7554/eLife.67075
25. Toyama BH, Savas JN, Park SK, Harris MS, Ingolia NT, Yates JR, 3rd, Hetzer MW (2013) Identification of long-lived proteins reveals exceptional stability of essential cellular structures. Cell 154 (5):971-982. doi:10.1016/j.cell.2013.07.037
26. Savas JN, Toyama BH, Xu T, Yates JR, 3rd, Hetzer MW (2012) Extremely long-lived nuclear pore proteins in the rat brain. Science 335 (6071):942. doi:10.1126/science.1217421
27. Cohen S, Kramarski L, Levi S, Deshe N, Ben David O, Arbely E (2019) Nonsense mutation-dependent reinitiation of translation in mammalian cells. Nucleic Acids Res 47 (12):6330-6338. doi:10.1093/nar/gkz319
28. Armenti ST, Lohmer LL, Sherwood DR, Nance J (2014) Repurposing an endogenous degradation system for rapid and targeted depletion of C. elegans proteins. Development 141 (23):4640-4647. doi:10.1242/dev.115048
29. Caussinus E, Kanca O, Affolter M (2011) Fluorescent fusion protein knockout mediated by anti-GFP nanobody. Nat Struct Mol Biol 19 (1):117-121. doi:10.1038/nsmb.2180
30. Matsushima W, Herzog VA, Neumann T, Gapp K, Zuber J, Ameres SL, Miska EA (2018) SLAM-ITseq: sequencing cell type-specific transcriptomes without cell sorting. Development 145 (13). doi:10.1242/dev.164640

31. Porta-de-la-Riva M, Gonzalez AC, Sanfeliu-Cerdán N, Karimi S, González-Bolívar S, Morales-Curiel LF, Hurth C, Krieg M (2021) Deploying photons for communication within neuronal networks. bioRxiv:2021.2008.2002.454613. doi:10.1101/2021.08.02.454613
32. Schwartz ML, Jorgensen EM (2016) SapTrap, a Toolkit for High-Throughput CRISPR/Cas9 Gene Modification in Caenorhabditis elegans. Genetics 202 (4):1277-1288. doi:10.1534/genetics.115.184275
33. Gomez-Saldivar G, Fernandez A, Hirano Y, Mauro M, Lai A, Ayuso C, Haraguchi T, Hiraoka Y, Piano F, Askjaer P (2016) Identification of Conserved MEL-28/ELYS Domains with Essential Roles in Nuclear Assembly and Chromosome Segregation. PLoS Genet 12 (6):e1006131. doi:10.1371/journal.pgen.1006131
34. Redemann S, Schloissnig S, Ernst S, Pozniakowsky A, Ayloo S, Hyman AA, Bringmann H (2011) Codon adaptation-based control of protein expression in C. elegans. Nat Methods 8 (3):250-252. doi:10.1038/nmeth.1565
35. Stiernagle T (2006) Maintenance of C. elegans. WormBook:1-11. doi:10.1895/wormbook.1.101.1
36. Frokjaer-Jensen C, Davis MW, Hopkins CE, Newman BJ, Thummel JM, Olesen SP, Grunnet M, Jorgensen EM (2008) Single-copy insertion of transgenes in Caenorhabditis elegans. Nat Genet 40 (11):1375-1383. doi:ng.248 [pii] 10.1038/ng.248
37. Dobrzynska A, Askjaer P, Gruenbaum Y (2016) Lamin-Binding Proteins in Caenorhabditis elegans. Methods in enzymology 569:455-483. doi:10.1016/bs.mie.2015.08.036
38. Frokjaer-Jensen C, Davis MW, Ailion M, Jorgensen EM (2012) Improved Mos1-mediated transgenesis in C. elegans. Nat Methods 9 (2):117-118. doi:10.1038/nmeth.1865
39. Rodenas E, Gonzalez-Aguilera C, Ayuso C, Askjaer P (2012) Dissection of the NUP107 nuclear pore subcomplex reveals a novel interaction with spindle assembly checkpoint protein MAD1 in Caenorhabditis elegans. Mol Biol Cell 23 (5):930-944. doi:10.1091/mbc.E11-11-0927
40. Friedland AE, Tzur YB, Esvelt KM, Colaiacovo MP, Church GM, Calarco JA (2013) Heritable genome editing in C. elegans via a CRISPR-Cas9 system. Nat Methods 10 (8):741-743. doi:10.1038/nmeth.2532
41. Schindelin J, Arganda-Carreras I, Frise E, Kaynig V, Longair M, Pietzsch T, Preibisch S, Rueden C, Saalfeld S, Schmid B, Tinevez JY, White DJ, Hartenstein V, Eliceiri K, Tomancak P, Cardona A (2012) Fiji: an open-source platform for biological-image analysis. Nat Methods 9 (7):676-682. doi:10.1038/nmeth.2019
42. Team R (2020) RStudio: Integrated Development Environment for R. 1.3.1093 edn.,
43. Team RC (2020) R: A Language and Environment for Statistical Computing.
44. Wickham H (2016) ggplot2: Elegant Graphics for Data Analysis. Springer-Verlag New York,
45. Kassambara A (2020) ggpubr: 'ggplot2' Based Publication Ready Plots. R package version 0.4.0 edn.,
46. Therneau T (2020) A Package for Survival Analysis in R. R package version 3.2-7 edn.,
47. Matsushima W, Herzog VA, Neumann T, Gapp K, Zuber J, Ameres SL, Miska EA (2019) Sequencing cell-type-specific transcriptomes with SLAM-ITseq. Nat Protoc 14 (8):2261-2278. doi:10.1038/s41596-019-0179-x

48. Neumann T, Herzog VA, Muhar M, von Haeseler A, Zuber J, Ameres SL, Rescheneder P (2019) Quantification of experimentally induced nucleotide conversions in high-throughput sequencing datasets. BMC Bioinformatics 20 (1):258. doi:10.1186/s12859-019-2849-7
49. Love MI, Huber W, Anders S (2014) Moderated estimation of fold change and dispersion for RNA-seq data with DESeq2. Genome Biol 15 (12):550. doi:10.1186/s13059-014-0550-8
50. Pham TV, Piersma SR, Warmoes M, Jimenez CR (2010) On the beta-binomial model for analysis of spectral count data in label-free tandem mass spectrometry-based proteomics. Bioinformatics 26 (3):363-369. doi:10.1093/bioinformatics/btp677
51. Van de Walle P, Munoz-Jimenez C, Askjaer P, Schoofs L, Temmerman L (2020) DamID identifies targets of CEH-60/PBX that are associated with neuron development and muscle structure in Caenorhabditis elegans. PLoS One 15 (12):e0242939. doi:10.1371/journal.pone.0242939
52. Kroetz MB, Zarkower D (2015) Cell-Specific mRNA Profiling of the Caenorhabditis elegans Somatic Gonadal Precursor Cells Identifies Suites of Sex-Biased and Gonad-Enriched Transcripts. G3 (Bethesda) 5 (12):2831-2841. doi:10.1534/g3.115.022517
53. Hubbard EJ, Greenstein D (2005) Introduction to the germ line. WormBook:1-4. doi:10.1895/wormbook.1.18.1
54. Tamai KK, Nishiwaki K (2007) bHLH transcription factors regulate organ morphogenesis via activation of an ADAMTS protease in C. elegans. Dev Biol 308 (2):562-571. doi:10.1016/j.ydbio.2007.05.024
55. Tan PB, Lackner MR, Kim SK (1998) MAP kinase signaling specificity mediated by the LIN-1 Ets/LIN-31 WH transcription factor complex during C. elegans vulval induction. Cell 93 (4):569-580. doi:S0092-8674(00)81186-1 [pii]
56. Reece-Hoyes JS, Shingles J, Dupuy D, Grove CA, Walhout AJ, Vidal M, Hope IA (2007) Insight into transcription factor gene duplication from Caenorhabditis elegans Promoterome-driven expression patterns. BMC genomics 8:27. doi:10.1186/1471-2164-8-27
57. Nehrke K, Melvin JE (2002) The NHX family of Na+-H+ exchangers in Caenorhabditis elegans. J Biol Chem 277 (32):29036-29044. doi:10.1074/jbc.M203200200
58. McGhee JD (2007) The C. elegans intestine. WormBook:1-36. doi:10.1895/wormbook.1.133.1
59. Altun ZF, Hall DH (2009) Coelomocyte system. WormAtlas. doi:10.3908/wormatlas.1.11
60. Loria PM, Hodgkin J, Hobert O (2004) A conserved postsynaptic transmembrane protein affecting neuromuscular signaling in Caenorhabditis elegans. The Journal of neuroscience : the official journal of the Society for Neuroscience 24 (9):2191-2201. doi:10.1523/JNEUROSCI.5462-03.2004
61. Arribere JA, Kuroyanagi H, Hundley HA (2020) mRNA Editing, Processing and Quality Control in Caenorhabditis elegans. Genetics 215 (3):531-568. doi:10.1534/genetics.119.301807
62. Gorjanacz M, Klerkx EP, Galy V, Santarella R, Lopez-Iglesias C, Askjaer P, Mattaj IW (2007) Caenorhabditis elegans BAF-1 and its kinase VRK-1 participate directly in post-mitotic nuclear envelope assembly. EMBO J 26 (1):132-143
63. Galy V, Askjaer P, Franz C, Lopez-Iglesias C, Mattaj IW (2006) MEL-28, a novel nuclear-envelope and kinetochore protein essential for zygotic nuclear-envelope assembly in C. elegans. Curr Biol 16 (17):1748-1756

1080 64. Fernandez AG, Piano F (2006) MEL-28 is downstream of the Ran cycle and is
1081 required for nuclear-envelope function and chromatin maintenance. Curr Biol 16
1082 (17):1757-1763
1083 65. Haenni S, Ji Z, Hoque M, Rust N, Sharpe H, Eberhard R, Browne C, Hengartner
1084 MO, Mellor J, Tian B, Furger A (2012) Analysis of C. elegans intestinal gene
1085 expression and polyadenylation by fluorescence-activated nuclei sorting and 3'-end-
1086 seq. Nucleic Acids Res 40 (13):6304-6318. doi:10.1093/nar/gks282
1087 66. Steiner FA, Talbert PB, Kasinathan S, Deal RB, Henikoff S (2012) Cell-type-
1088 specific nuclei purification from whole animals for genome-wide expression and
1089 chromatin profiling. Genome Res 22 (4):766-777. doi:10.1101/gr.131748.111
1090 67. Kaletsky R, Yao V, Williams A, Runnels AM, Tadych A, Zhou S, Troyanskaya
1091 OG, Murphy CT (2018) Transcriptome analysis of adult Caenorhabditis elegans cells
1092 reveals tissue-specific gene and isoform expression. PLoS Genet 14 (8):e1007559.
1093 doi:10.1371/journal.pgen.1007559
1094 68. Blazie SM, Geissel HC, Wilky H, Joshi R, Newbern J, Mangone M (2017)
1095 Alternative Polyadenylation Directs Tissue-Specific miRNA Targeting in
1096 Caenorhabditis elegans Somatic Tissues. Genetics 206 (2):757-774.
1097 doi:10.1534/genetics.116.196774
1098 69. Ma X, Zhan G, Sleumer MC, Chen S, Liu W, Zhang MQ, Liu X (2016) Analysis of
1099 C. elegans muscle transcriptome using trans-splicing-based RNA tagging (SRT).
1100 Nucleic Acids Res 44 (21):e156. doi:10.1093/nar/gkw734
1101 70. Katsanos D, Ferrando-Marco M, Razzaq I, Aughey G, Southall TD, Barkoulas M
1102 (2021) Gene expression profiling of epidermal cell types in C. elegans using
1103 Targeted DamID. Development 148 (17). doi:10.1242/dev.199452
1104 71. Li J, Huang S, Chen J, Yang Z, Fei X, Zheng M, Ji C, Xie Y, Mao Y (2007)
1105 Identification and characterization of human uracil phosphoribosyltransferase
1106 (UPRTase). J Hum Genet 52 (5):415-422. doi:10.1007/s10038-007-0129-2
1107 72. Herzog VA, Reichholf B, Neumann T, Rescheneder P, Bhat P, Burkard TR,
1108 Wlotzka W, von Haeseler A, Zuber J, Ameres SL (2017) Thiol-linked alkylation of
1109 RNA to assess expression dynamics. Nat Methods 14 (12):1198-1204.
1110 doi:10.1038/nmeth.4435
1111 73. Packer JS, Zhu Q, Huynh C, Sivaramakrishnan P, Preston E, Dueck H, Stefanik
1112 D, Tan K, Trapnell C, Kim J, Waterston RH, Murray JI (2019) A lineage-resolved
1113 molecular atlas of C. elegans embryogenesis at single-cell resolution. Science.
1114 doi:10.1126/science.aax1971
1115 74. Cao J, Packer JS, Ramani V, Cusanovich DA, Huynh C, Daza R, Qiu X, Lee C,
1116 Furlan SN, Steemers FJ, Adey A, Waterston RH, Trapnell C, Shendure J (2017)
1117 Comprehensive single-cell transcriptional profiling of a multicellular organism.
1118 Science 357 (6352):661-667. doi:10.1126/science.aam8940
1119 75. Kimble J, Seidel H (2008) C. elegans germline stem cells and their niche. In:
1120 StemBook. Cambridge (MA). doi:10.3824/stembook.1.95.1
1121 76. Pereira L, Kratsios P, Serrano-Saiz E, Sheftel H, Mayo AE, Hall DH, White JG,
1122 LeBoeuf B, Garcia LR, Alon U, Hobert O (2015) A cellular and regulatory map of the
1123 cholinergic nervous system of C. elegans. Elife 4. doi:10.7554/eLife.12432
1124 77. Bhoi A, Palladino F, Fabrizio P (2021) Auxin confers protection against ER stress
1125 in Caenorhabditis elegans. Biol Open 10 (2). doi:10.1242/bio.057992
1126 78. Wurmthaler LA, Sack M, Gense K, Hartig JS, Gamerdinger M (2019) A
1127 tetracycline-dependent ribozyme switch allows conditional induction of gene
1128 expression in Caenorhabditis elegans. Nature communications 10 (1):491.
1129 doi:10.1038/s41467-019-08412-w

1130 79. Monsalve GC, Yamamoto KR, Ward JD (2019) A New Tool for Inducible Gene
1131 Expression in Caenorhabditis elegans. Genetics 211 (2):419-430.
1132 doi:10.1534/genetics.118.301705
1133 80. Garcia-Gonzalez AP, Ritter AD, Shrestha S, Andersen EC, Yilmaz LS, Walhout
1134 AJM (2017) Bacterial Metabolism Affects the C. elegans Response to Cancer
1135 Chemotherapeutics. Cell 169 (3):431-441 e438. doi:10.1016/j.cell.2017.03.046
1136 81. Andersen PS, Frees D, Fast R, Mygind B (1995) Uracil uptake in Escherichia coli
1137 K-12: isolation of uraA mutants and cloning of the gene. J Bacteriol 177 (8):2008-
1138 2013. doi:10.1128/jb.177.8.2008-2013.1995

1139

Figure 1

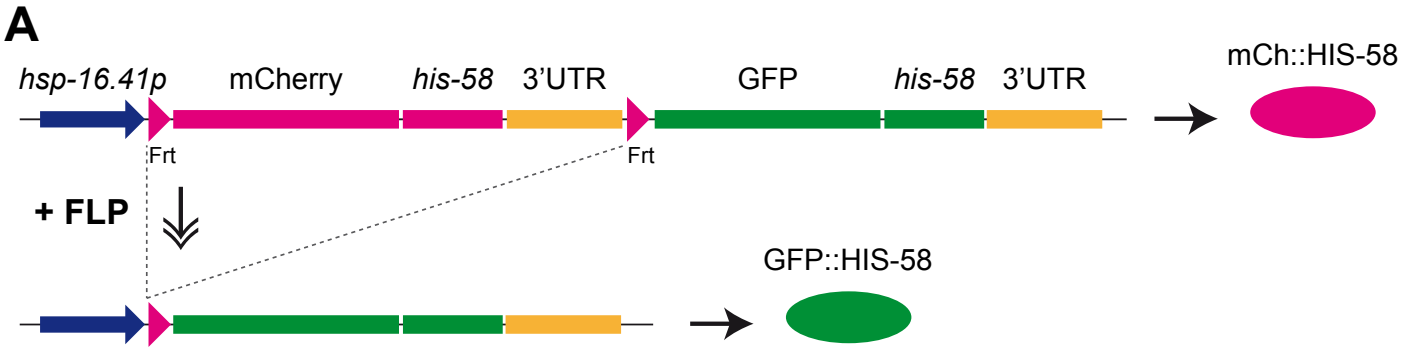

B

a' ckb-3p::FLP::SL2::mNG
Z1
Z4

a'' ckb-3p::FLP::SL2::mNG

b' hlh-12p::FLP::SL2::mNG
DTC

b'' hlh-12p::FLP::SL2::mNG
DTC

c' lin-31p::FLP::SL2::mNG
P1.p
P2.p
P3.p
P4.p
P5.p
P6.p
P7.p

c'' lin-31p::FLP::SL2::mNG
P1.p
P2.p
P3.p
P4.p
vulA-F

d' nhx-2p::FLP::SL2::mNG

d'' nhx-2p::FLP::SL2::mNG

e' unc-122p::FLP::SL2::mNG
ccPR+ccAR
ccPL+ccAL

e'' unc-122p::FLP::SL2::mNG
ccDL
ccDR

Figure 2

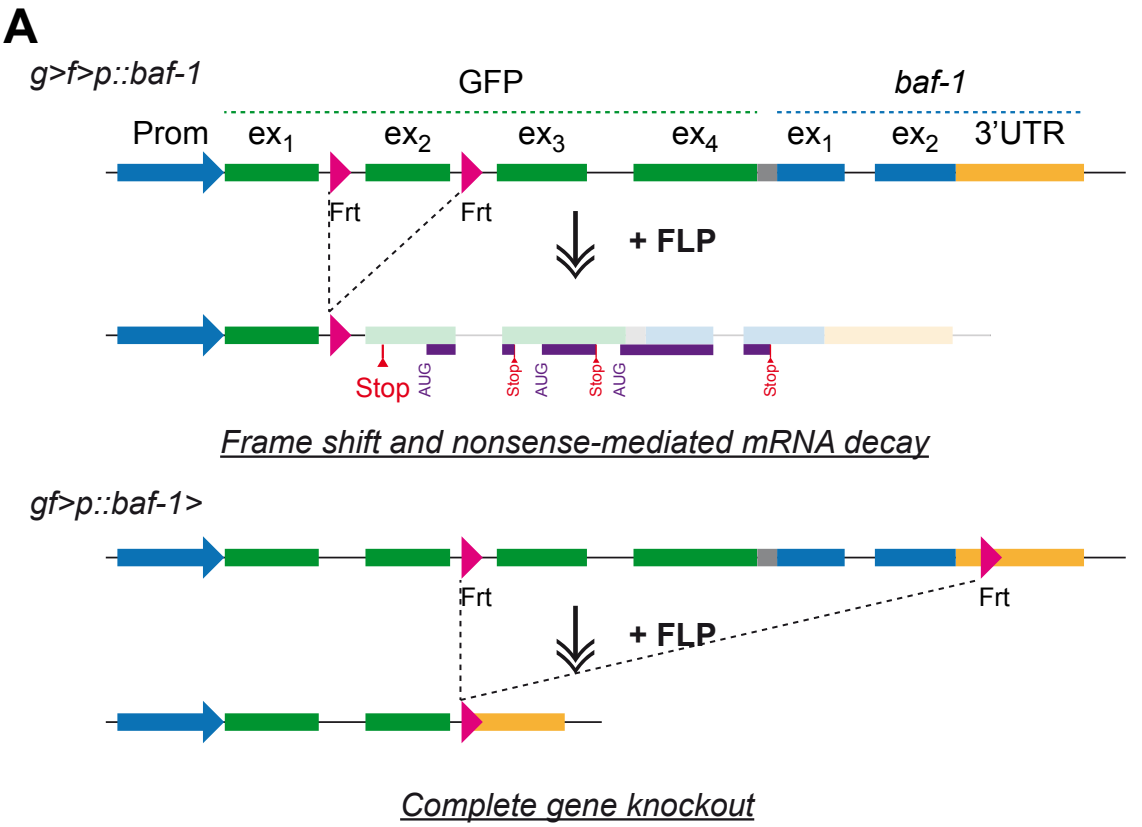
A
g>f>p::baf-1
GFP
baf-1
Prom
ex1
ex2
ex3
ex4
ex1
ex2
3'UTR
Frt
Frt
+ FLP
Stop
AUG
Stop
AUG
Stop
AUG
Stop
Frame shift and nonsense-mediated mRNA decay
gf>p::baf-1>
Frt
Frt
+ FLP
Complete gene knockout

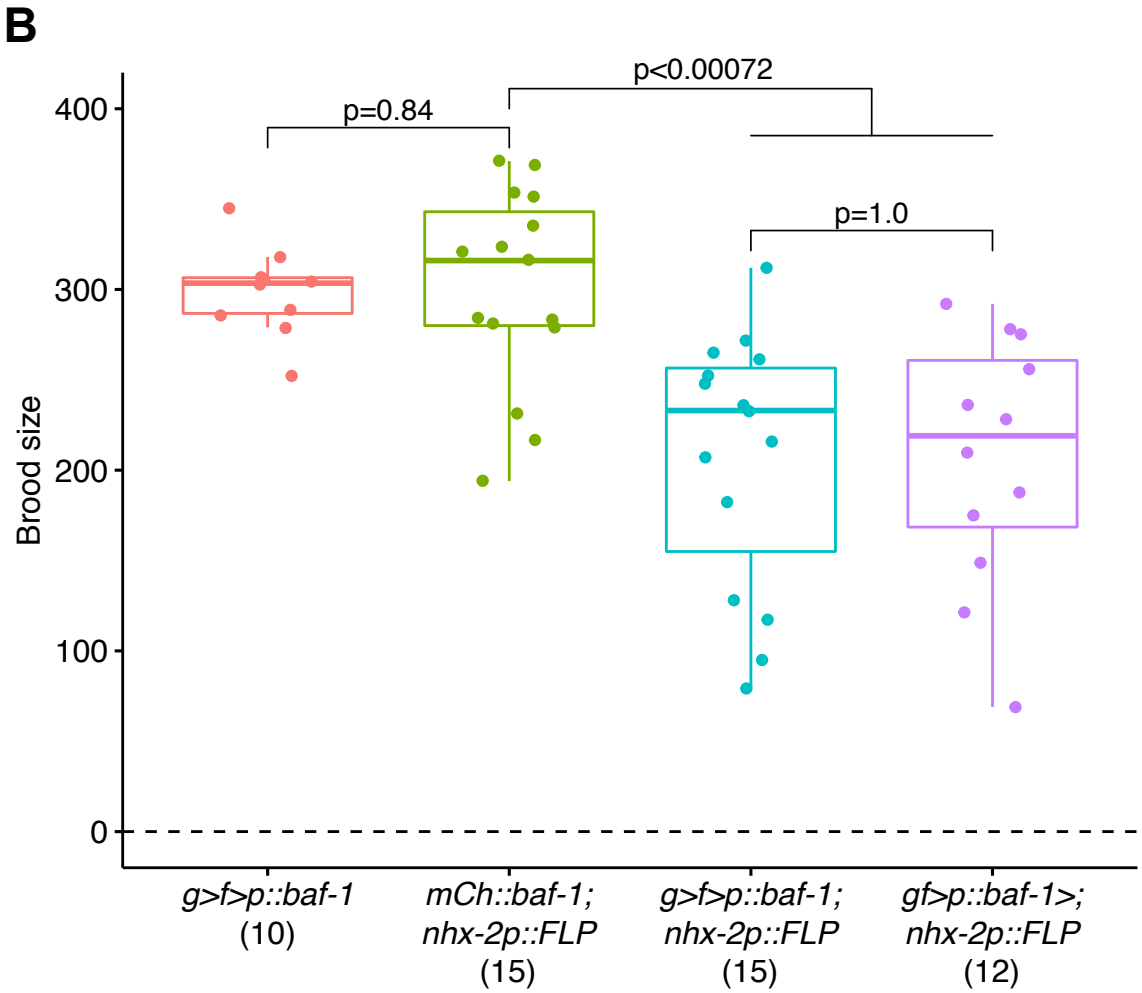
B
p<0.00072
p=0.84
p=1.0
Brood size
400
300
200
100
0
g>f>p::baf-1
(10)
mCh::baf-1;
nhx-2p::FLP
(15)
g>f>p::baf-1;
nhx-2p::FLP
(15)
gf>p::baf-1>;
nhx-2p::FLP
(12)

Figure 3

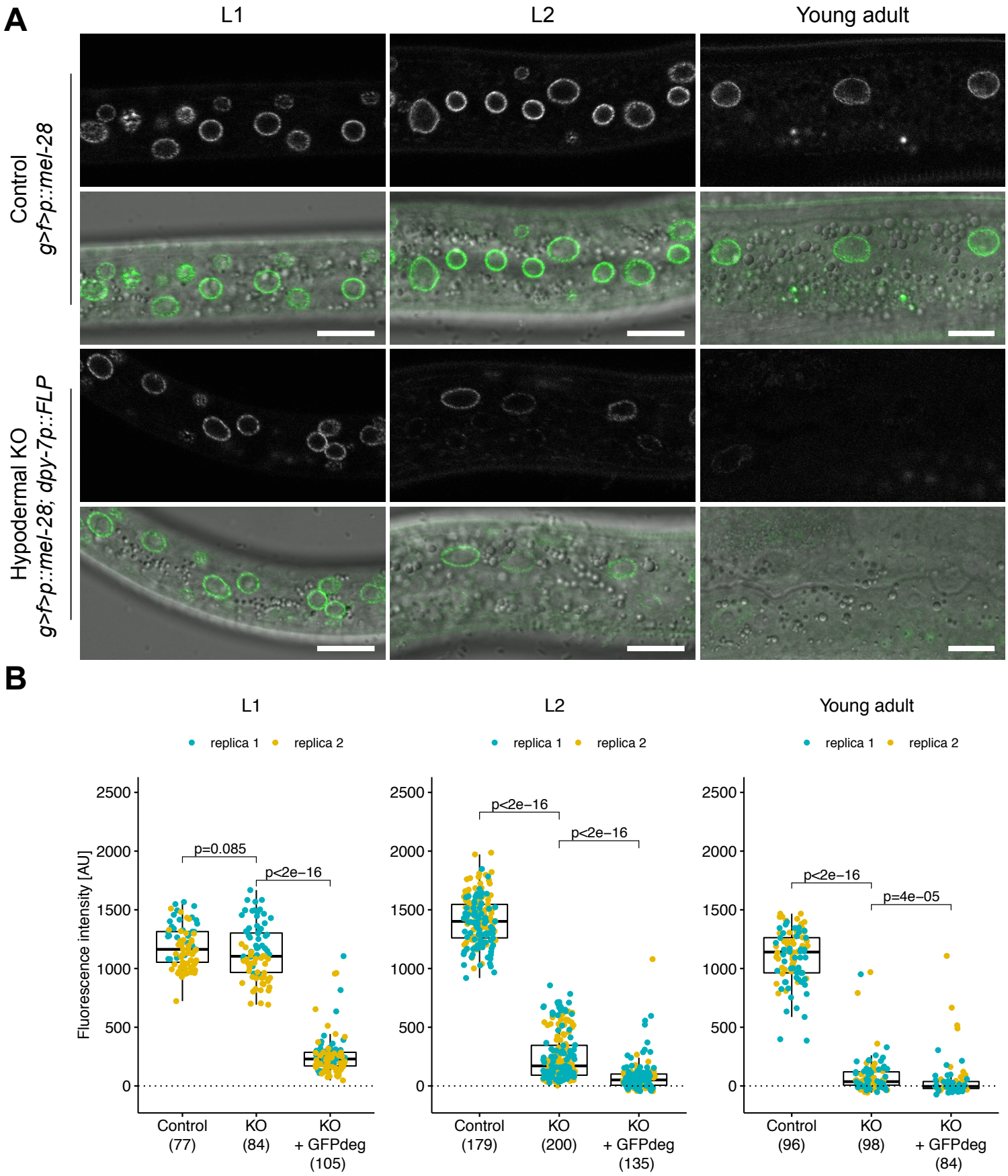
A
L1
L2
Young adult
Control
g>f>p::mel-28
Hypodermal KO
g>f>p::mel-28; dpy-7p::FLP
B
L1
L2
Young adult
replica 1
replica 2
Fluorescence intensity [AU]
2500
2000
1500
1000
500
0
p=0.085
p<2e−16
p<2e−16
p<2e−16
p<2e−16
p=4e−05
Control (77)
KO (84)
KO + GFPdeg (105)
Control (179)
KO (200)
KO + GFPdeg (135)
Control (96)
KO (98)
KO + GFPdeg (84)

Figure 4

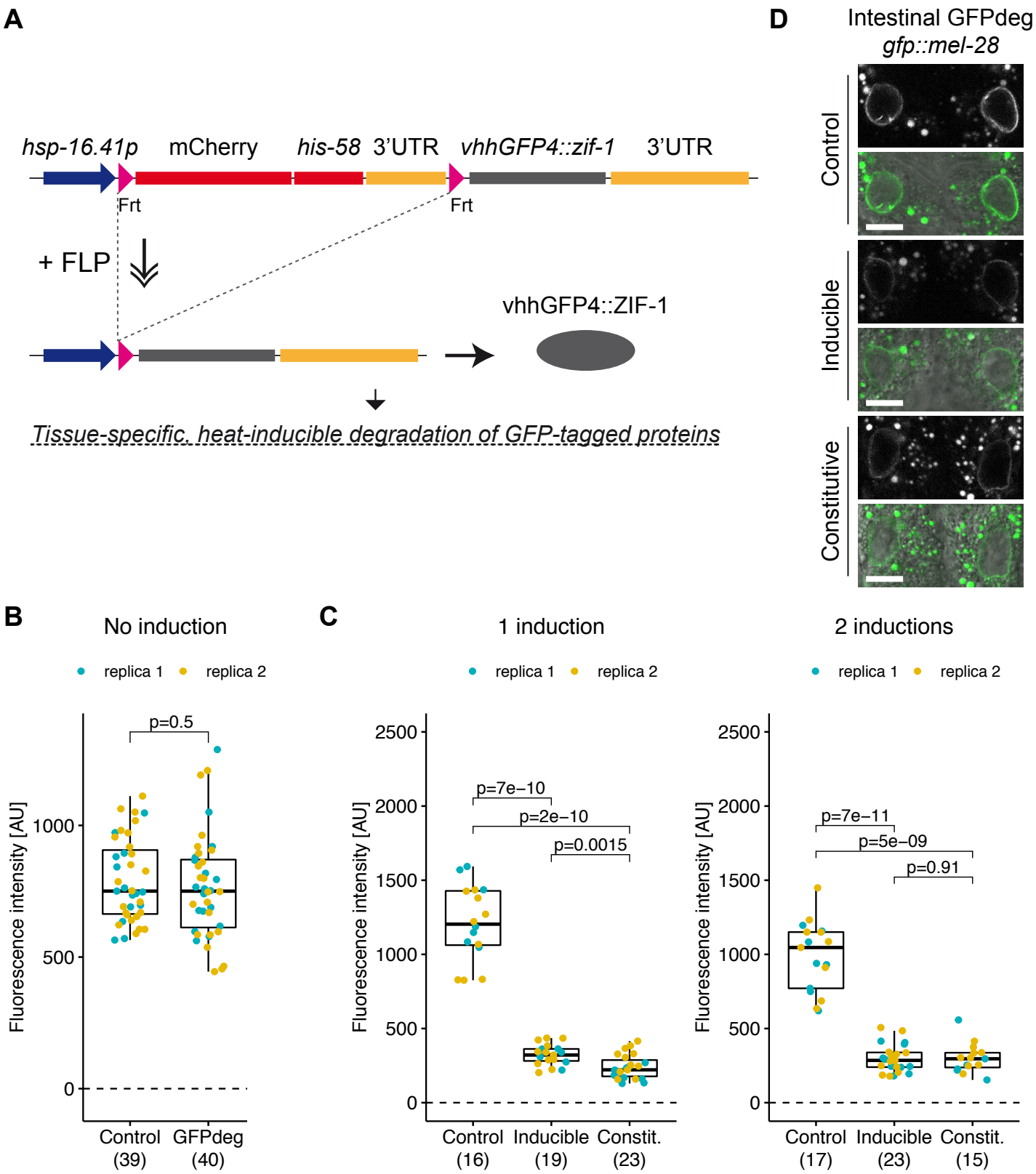
A
hsp-16.41p
mCherry
his-58 3'UTR
vhhGFP4::zif-1
3'UTR
Frt
Frt
+ FLP
vhhGFP4::ZIF-1
Tissue-specific, heat-inducible degradation of GFP-tagged proteins
D
Intestinal GFPdeg
gfp::mel-28
Control
Inducible
Constitutive
B
No induction
replica 1
replica 2
p=0.5
Fluorescence intensity [AU]
Control (39)
GFPdeg (40)
C
1 induction
p=7e−10
p=2e−10
p=0.0015
Control (16)
Inducible (19)
Constit. (23)
2 inductions
p=7e−11
p=5e−09
p=0.91
Control (17)
Inducible (23)
Constit. (15)

Figure 5

A

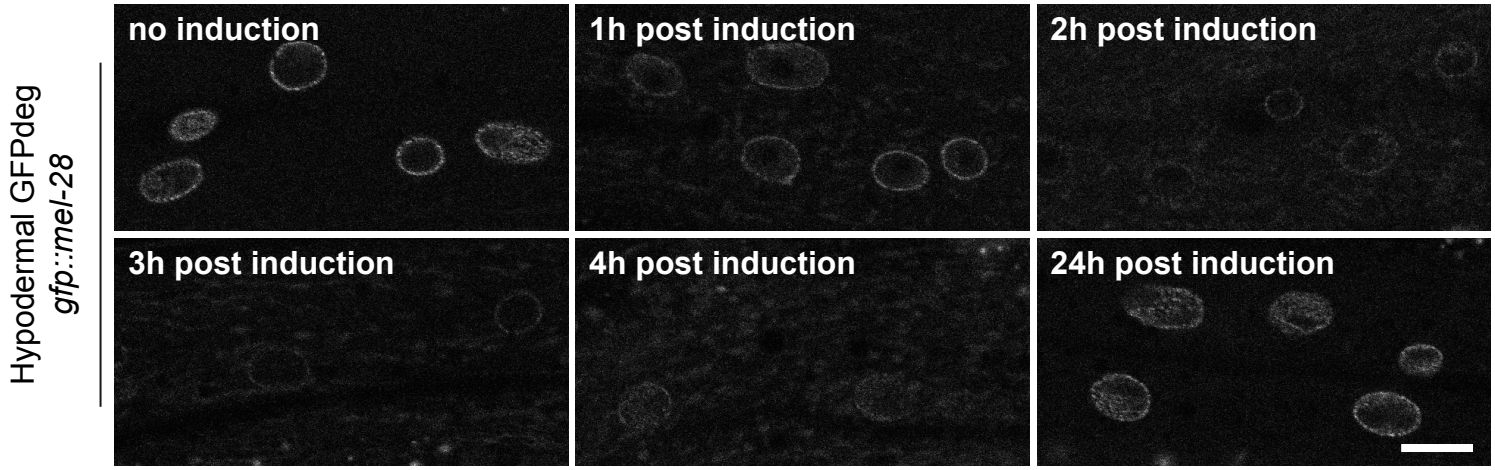
Hypodermal GFPdeg
gfp::mel-28
no induction
1h post induction
2h post induction
3h post induction
4h post induction
24h post induction

B

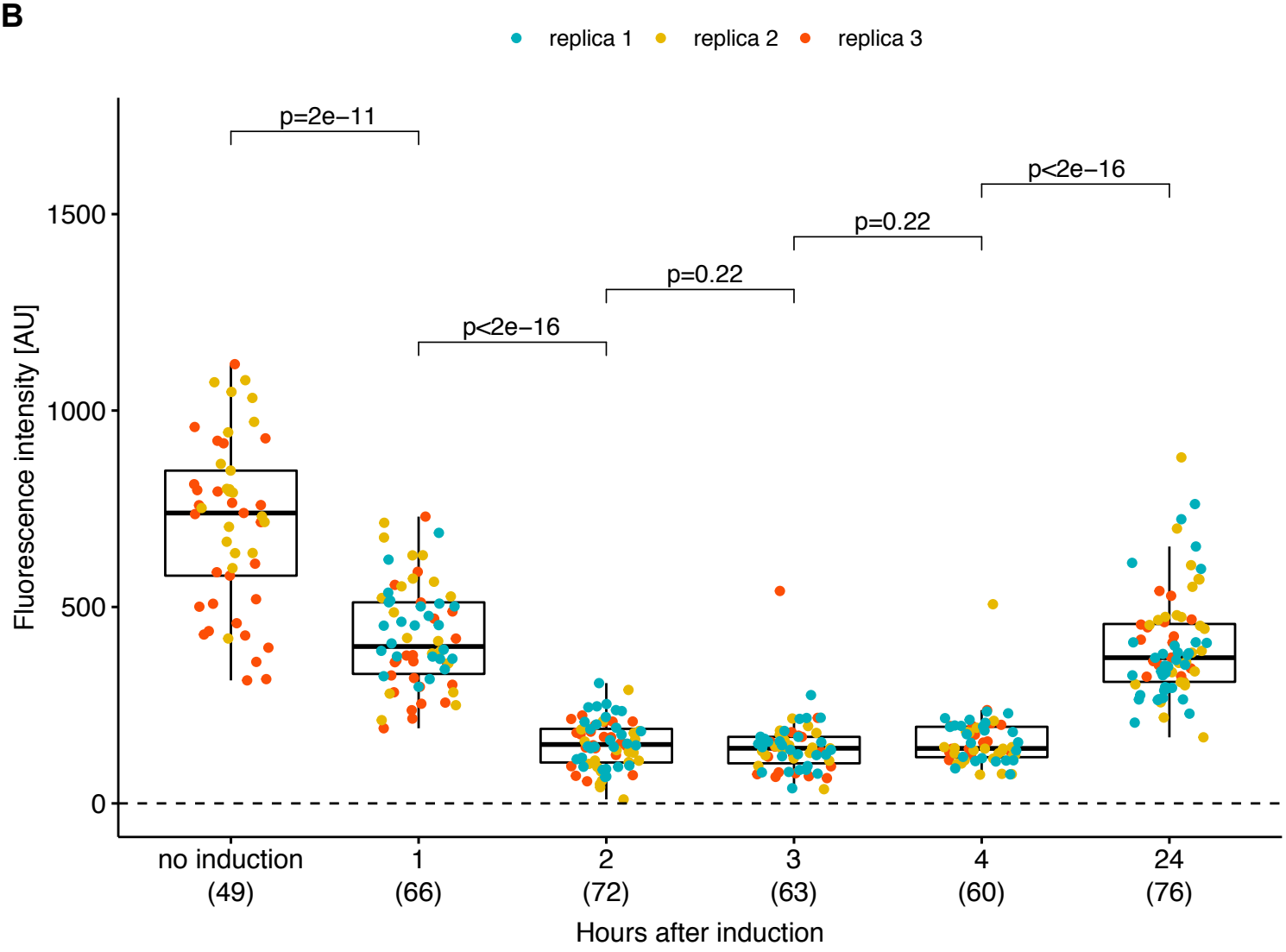
replica 1
replica 2
replica 3
p=2e−11
p<2e−16
p=0.22
p=0.22
p<2e−16
Fluorescence intensity [AU]
0
500
1000
1500
no induction (49)
1 (66)
2 (72)
3 (63)
4 (60)
24 (76)
Hours after induction

Figure 6

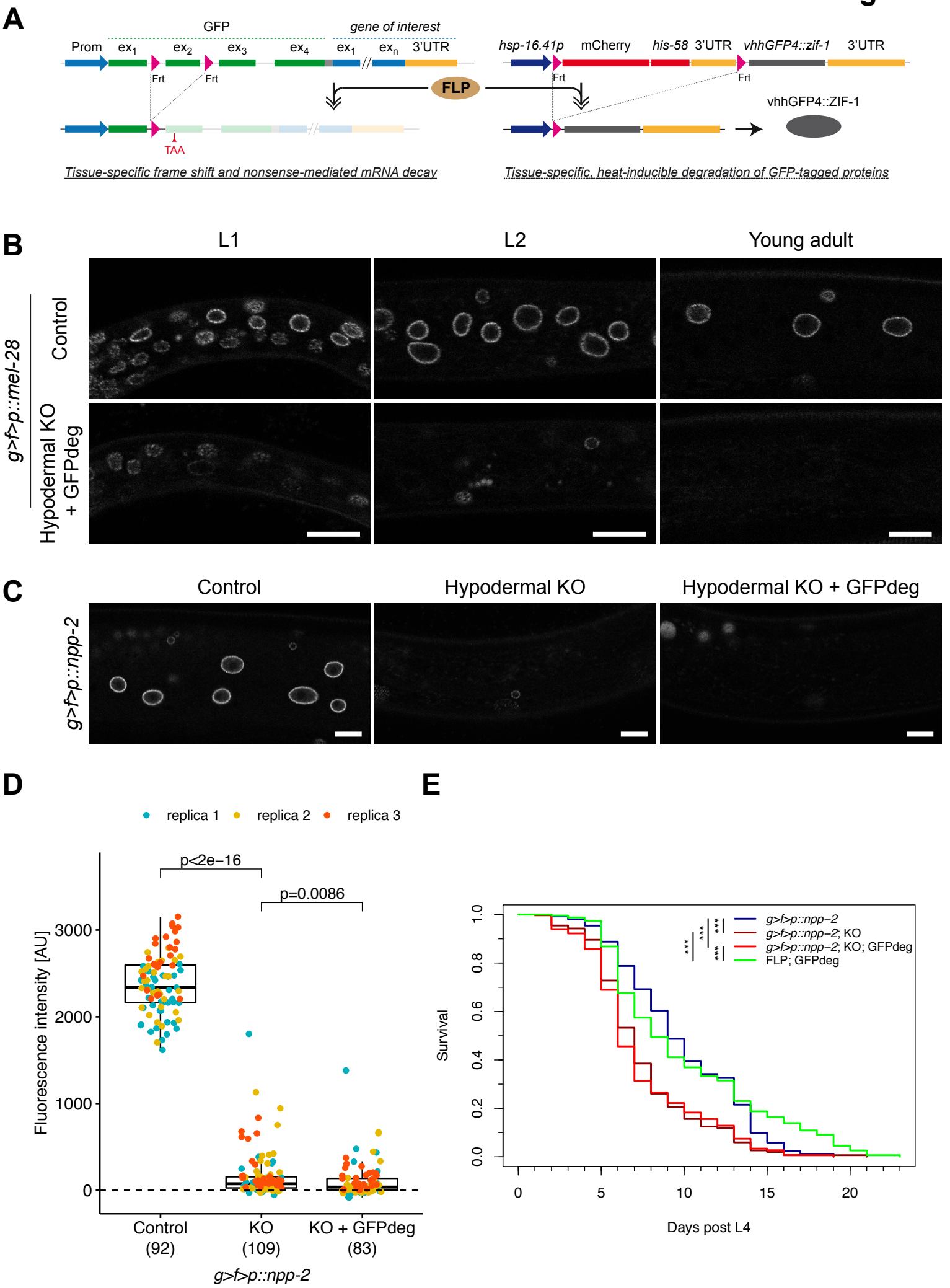
A
GFP
gene of interest
Prom
ex1
ex2
ex3
ex4
ex1
exn
3'UTR
Frt
Frt
TAA
FLP
hsp-16.41p
mCherry
his-58
3'UTR
vhhGFP4::zif-1
3'UTR
Frt
Frt
vhhGFP4::ZIF-1
Tissue-specific frame shift and nonsense-mediated mRNA decay
Tissue-specific, heat-inducible degradation of GFP-tagged proteins
B
L1
L2
Young adult
g>f>p::mel-28
Control
Hypodermal KO + GFPdeg
C
Control
Hypodermal KO
Hypodermal KO + GFPdeg
g>f>p::npp-2
D
replica 1
replica 2
replica 3
p<2e−16
p=0.0086
Fluorescence intensity [AU]
3000
2000
1000
0
Control (92)
KO (109)
KO + GFPdeg (83)
g>f>p::npp-2
E
Survival
1.0
0.8
0.6
0.4
0.2
0.0
0
5
10
15
20
Days post L4
g>f>p::npp−2
g>f>p::npp−2; KO
g>f>p::npp−2; KO; GFPdeg
FLP; GFPdeg
***
***
***
***

Figure 7

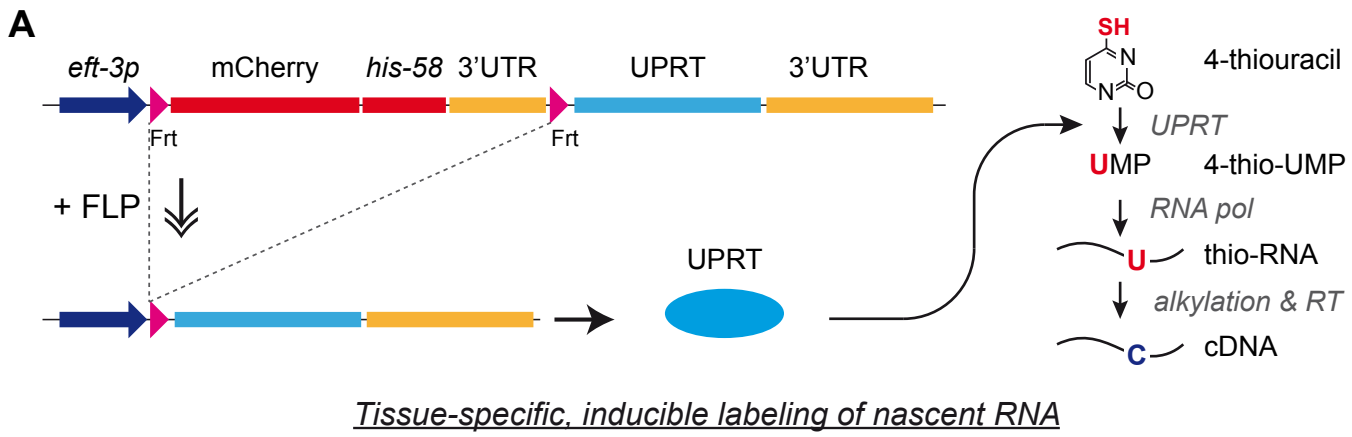
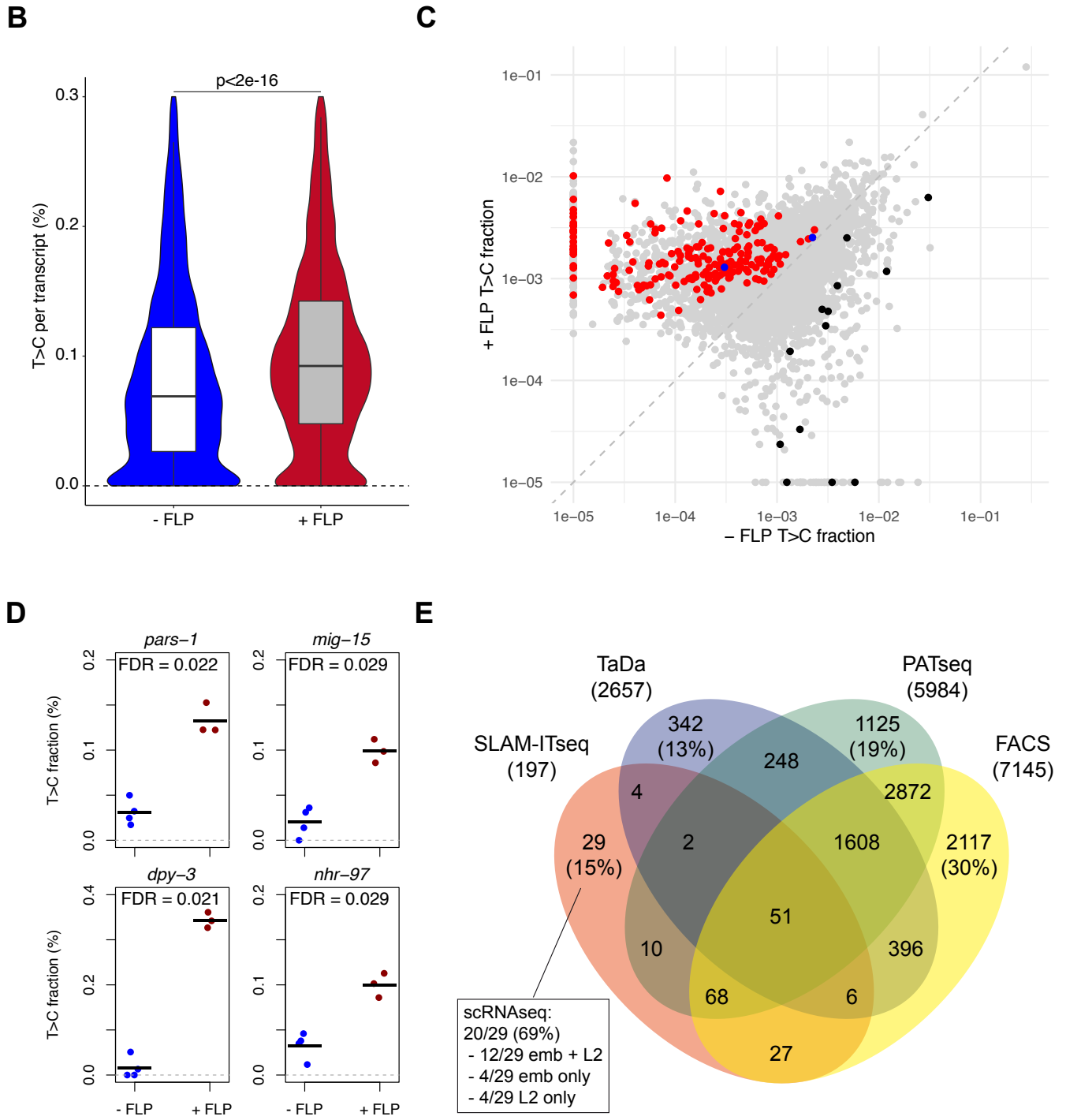
Tissue-specific, inducible labeling of nascent RNA